Physics – Uspekhi **66** (5) 494 – 517 (2023)

REVIEWS OF TOPICAL PROBLEMS PACS numbers: 42.25.Bs, 42.25.Fx, 42.79.Dj, 42.82.Et

Bound states in the continuum in photonic structures

K L Koshelev, Z F Sadrieva, A A Shcherbakov, Yu S Kivshar, A A Bogdanov

DOI: https://doi.org/10.3367/UFNe.2021.12.039120

Contents

Abstract. Bound states in the continuum (BICs) are a striking example of how a solution to a simple problem of quantum mechanics, obtained about a century ago, can serve as an incentive to study a wide range of resonance phenomena in wave physics. Due to the giant radiative lifetime, BICs have found multiple applications in various fields of physics studying wave processes, in particular, in hydrodynamics, atomic physics, and acoustics. In this review, we present a broad view of the physics of BICs and related effects, focusing primarily on photonic dielectric structures. We consider the history of the development of BIC studies, the main physical mechanisms of their formation, and specific examples of structures that can support such states. We also discuss possible practical applications of BICs in optics, photonics, and radiophysics.

Keywords: bound states in the continuum, metasurfaces, resonators, Fano resonance, diffraction structures, nanophotonics

K L Koshelev [(1)], **Z F Sadrieva** [(2)], **A A Shcherbakov** [(2)], **Yu S Kivshar** [(1)], **A A Bogdanov** [(2, 3, *)]
[(1)] Nonlinear Physics Centre, Research School of Physics, Australian National University, Mills Road, Building 59, 2600 Canberra, Australia
[(2)] School of Physics and Engineering, ITMO University, Kronverksky prosp. 49/A, 197101 St. Petersburg, Russian Federation
[(3)] Harbin Engineering University, Qingdao Innovation and Development Center, Sansha road 1777, 266000 Qingdao, Shandong, China
E-mail: [(*)] a.bogdanov@metalab.ifmo.ru

Received 30 August 2021, revised 5 December 2021
Uspekhi Fizicheskikh Nauk **193** (5) 528 – 553 (2023)
Translated by V L Derbov

1. Introduction

One of the basic problems in quantum mechanics is the energy eigenvalue for a particle in a spherical quantum well. For energies below the potential barrier ($E < 0$), the spectrum is discrete and the wave functions are bounded, i.e., $\int_{\mathcal{R}^3} |\psi(\mathbf{r})|^2 \, \mathrm{d}\mathbf{r} < \infty$. Above the barrier ($E > 0$), the spectrum is continuous and the wave functions cannot be normalized in the classical sense (Fig. 1a). Then, the quantum mechanical problem solutions can be presented as propagating modes of the free space surrounding the quantum well. However, E Wigner and J von Neumann [1] found in 1929 that this classification can be violated for specific potentials that asymptotically tend to zero away from the quantum well. As shown by the authors of Ref. [1], for some potentials, the bound states can be found embedded in the continuum of propagating modes (Fig. 1b). At present, such modes are known as *bound states in the continuum* (BICs). To all appearances, this term was first introduced by L Fonda in 1960 [2]. We should mention that the paper by E Wigner and J von Neumann contains an algebraic error that was noticed and corrected by Stillenger and Herrick [3]. Later, the theory of BICs was generalized to describe various atomic, molecular, and quantum mechanical systems [3–10]; however, the potential of a rather specific form proposed by E Wigner and J von Neumann has been never implemented. Ideas on how to construct potentials supporting BICs in semiconductor superlattices developed in Refs [11, 12] were not implemented experimentally either. We should mention that experiment [13] has nothing in common with the observation of BICs in semiconductor superlattices. The authors of [13] simply observed a defect state in the band gap spatially localized by electron Bragg reflectors.

BICs are not a unique feature of quantum mechanical systems. On the contrary, they are essentially particular solutions of any wave equations and can exist in acoustics, hydrodynamics, aerodynamics [14–20], and optics [21, 22]. In

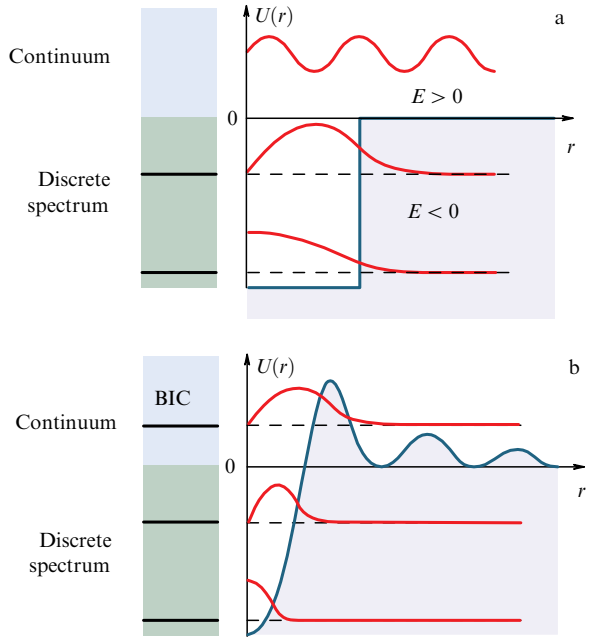

Figure 1. (a) Spherical quantum well: spectrum is continuous for $E > 0$ and discrete for $E < 0$. (b) Specific potential $U(r)$ giving rise to the appearance of bound states in the continuum.

acoustics and hydrodynamics, BICs have been known for a long time as *trapped modes*.

In recent years, BICs were actively studied in the areas of optics and photonics, as these states open up promising opportunities for implementing compact high-Q resonators and metasurfaces required for biosensing, enhancing nonlinear optical effects, and light-matter interaction. During the last few years, several reviews of the state-of-the-art achievements in BICs have been published [23–27].

In this review, we focus on BICs in electrodynamic systems in various spectral ranges, including visible, infrared, terahertz, and microwave. History, modern achievements, and various physical models explaining the nature of this beautiful phenomenon are presented. In Section 2, the history of BICs in optics is described, and a selection of pioneering scientific papers is presented, including those that were published before the introduction of the term 'optical bound states in the continuum.' Section 3 is devoted to the description of various mechanisms of BIC formation in dielectric structures. Their quantum-mechanical nature, the importance and role of potential periodicity for BIC implementation, and topological properties are discussed. It is also shown how the properties of BICs can be explained in terms of multipole analysis. In Section 4, examples of photonic structures with BICs are presented, and features of BICs are described in structures of various dimensionality: from single nanoparticles to periodic metasurfaces. In this section, we also briefly talk about quasi-BICs, which are formed from BICs due to the violation of symmetry in a photonic structure. In Section 5, applications of BICs are discussed for detecting biological objects and generating laser radiation, twisted light beams, and optical harmonics.

2. Historical reference

In the modern literature, it is widely believed that BICs in optical systems were predicted in 2008 in two papers: by Marinica, Borisov, and Shabanov [21], and by Bulgakov and Sadreev [22], and that the first experiment demonstrating BICs in optics was performed in 2011 and reported in Ref. [28]. The authors of Ref. [21] considered two examples of similar periodic photonic structures supporting BICs. One of these structures is a two-layer dielectric grating periodic along the x-axis and possessing translation symmetry along the y-axis (Fig. 2). The authors showed that, at certain distances between the gratings, the resonances in the reflection spectrum at oblique incidence become infinitely narrow and disappear from the spectrum. The authors of [21] also mentioned that this state corresponds to the ideal propagation of light along the structure without radiation losses. At the same time, Bulgakov and Sadreev [22] considered a single-mode waveguide formed by two identical photonic crystals and showed that light can be perfectly trapped in defects of a photonic crystal despite the fact that the frequency of the trapped mode lies in the transmission band of the waveguide. Figure 2c shows the spectra of waveguide transmission for various parameters of the defects (solid and dashed curve). The solid curve corresponds to the near-BIC case, when the Fano resonance collapses. The inset in Fig. 2c shows the field distribution at the minimum of the transmission spectrum.

Plotnik et al. [28] performed an elegant experiment on the observation of symmetry-protected BICs in a photonic structure consisting of an array of parallel dielectric single-mode waveguides fabricated of fused silica by direct laser writing (Fig. 2d). The near-field coupling between the waveguides results in the formation of a transmission band. Two additional waveguides fabricated above and below the array support the antisymmetric mode with a frequency lying in the transmission band of the waveguide array. This antisymmetric mode was excited from one side of the sample, and the intensity distribution was observed on the other side. The lower panel in Fig. 2d shows that the energy of the initial antisymmetric mode does not leak to the waveguide array. In order to break the vertical symmetry, a gradient of the refractive index along the vertical axis was created by heating the top side of the sample with simultaneous cooling of the bottom. Such heating results in the coupling of the excited anti-symmetric mode to the modes of the array. Thus, as the mode propagates through the sample, its energy is distributed between the waveguides forming the array.

Here, it should be emphasized that it was the above papers [21, 22, 28] that first demonstrated the explicit relation between BICs in quantum mechanics and BICs in optics. However, there are many earlier publications, where electromagnetic BICs were studied theoretically and experimentally but were not associated with quantum mechanics and pioneering study [1].

To the best of our knowledge, the history of BICs in optics began in 1976 with the work of Kazarinov, Sokolova, and Suris [29],who considered a corrugated waveguide playing the role of a distributed-feedback resonator of a semiconductor laser and noticed that, if the eigenmode in the center of the Brillouin zone is formed by two counterpropagating waves with a phase difference of π, then its radiation losses are zero. Independent of [29], Vincent and Nevière considered theoretically the band structure of a dielectric corrugated waveguide (Fig. 3) [30]. As shown by the authors of Ref. [30], the coupling of some resonances with the radiation continuum can be completely broken at the Γ point of k space due to the symmetry mismatch between the mode and the external field, which leads to an infinite radiative lifetime. The authors of Refs [29, 30] did not associate the observed resonances with

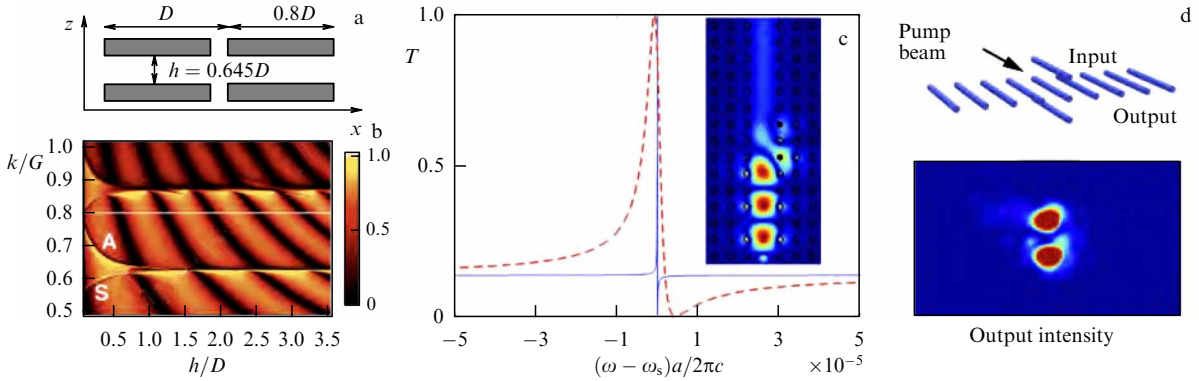

Figure 2. (a) Schematic of a double grating structure in a vacuum (D is the grating period). (b) Specular reflection coefficient as a function of wave vector k of the incident radiation and distance h between the gratings for the fixed value of $k_x = 0.2G$ (where G is the reciprocal grating vector), A is the antisymmetric mode, S is the symmetric mode. (Adapted from [21]). (c) Probability of transmission T of a propagating photonic mode as a function of exciting field frequency ω ($\omega_s a/(2\pi c) = 0.3753$, where a is the grating period, c is the speed of light) in the vicinity of the BIC for two sets of permittivity values in the structure. Inset demonstrates the mode profile. (Adapted from [22].) (d) Schematic of a uniform one-dimensional grating of 51 waveguides and two additional waveguides above and below the grating. Lower part of Fig. (d) shows the light intensity at the output plane of the structure. (Adapted from [28].)

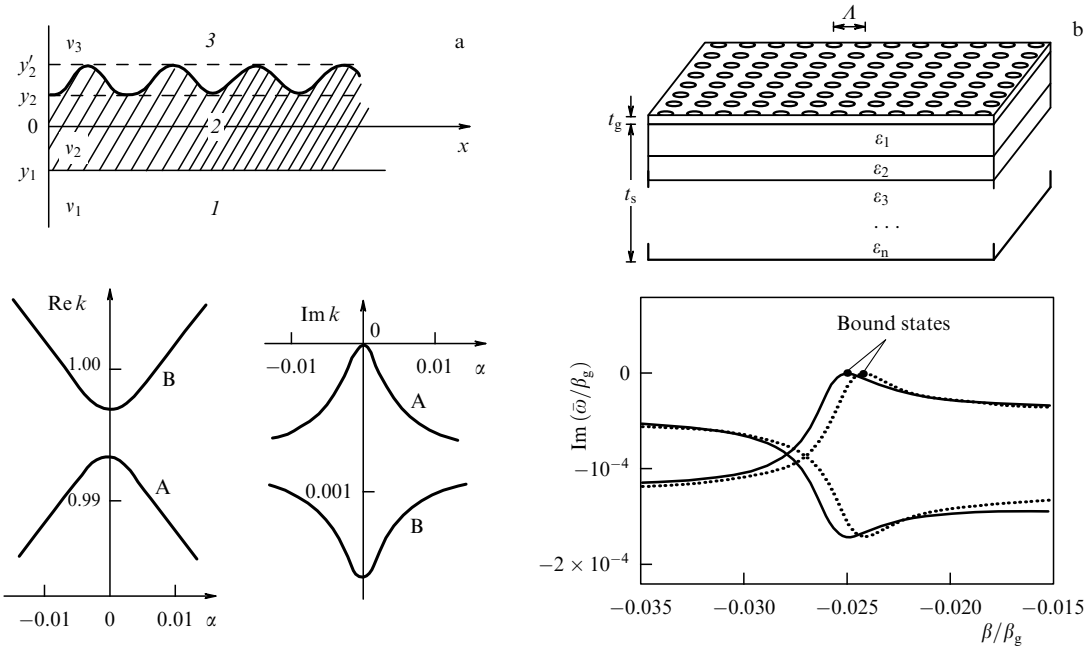

Figure 3. (a) Schematic image of a corrugated waveguide (top) and dispersion curves for the normalized frequency corresponding to two branches: antisymmetric (A) and symmetric (B) (bottom). *1*, *2*, *3* are regions with different materials, v_1, v_2, and v_3 are refractive indices of these regions, α is the constant of propagation along the x-axis. (Adapted from [30].) (b) Schematic of a multilayer slab waveguide with two-dimensional periodic texture (top) and the imaginary part of the frequency near the anti-crossing between TE-like and TM-like modes. Imaginary part of the frequency turns into zero for higher-energy band-edge states near the anti-crossing, indicating a truly bound state (bottom). Λ is the grating step, t_g is the grating thickness, β is the constant of propagation along the x-axis, β_g is the reciprocal grating vector. (Adapted from [31].)

BICs, nor did they recognize the relation with earlier studies in the field of quantum mechanics, but the physics of nonradiating states were studied thoroughly.

Nonradiative states were also found in a two-dimensional periodic array of coupled dielectric spheres by M Inoue et al. [32]. They showed that, at the center of the Brillouin zone, optically inactive states exist that cannot be excited by a normally incident wave, regardless of its polarization. However, such states can be excited at oblique incidence, and, in this case, extremely narrow peaks appear in the reflection/transmission spectrum (Fig. 4a). The existence of nonradiating modes in photonic crystal structures was also discussed by K Sakoda [33, 34] and later by P Paddon and J Young [31, 35]. The latter two developed a method based on Green's functions that allows analyzing a complex photonic band structure, i.e., the spectral positions of resonances and their radiative lifetimes (Fig. 3b). Probably, [31] is the first paper where BICs with a nonzero Bloch wavenumber, so-called *parametric*, *tunable*, or *accidental* BICs, were theoretically predicted. The authors explained that the coupling between the TE and TM modes leads to the anticrossing of their dispersion curves and the formation of a mode with zero imaginary part of its eigenfrequency, i.e., the formation of a BIC. In fact, the described mechanism is identical to that analyzed in the paper by H Friedrich and D Wintgen [7] for quantum mechanical systems. Therefore, accidental BICs are also called Friedrich–Wintgen BICs. In 2003, S Shipman and S Venakides also observed BICs numerically in the spectra of

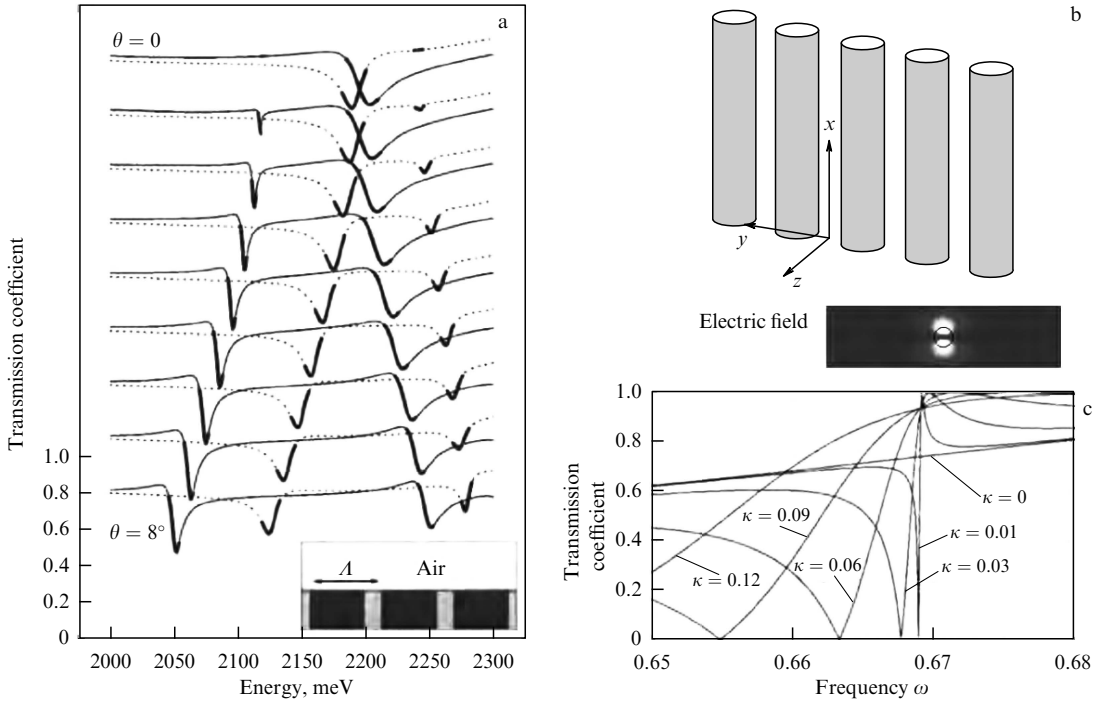

Figure 4. (a) Transmission spectra of a polaritonic crystal slab shown in the inset. Spectra are calculated for different angles of incidence in the narrow energy interval around the fourth Bragg resonance of the lower polaritonic branch. Solid line — incident wave is polarized along the grooves (s-polarization). Dotted line — incident wave is polarized orthogonal to the grooves (p-polarization). (Adapted from [38]). (b) Schematic of a two-dimensional multilayer periodic slab. Lower part of the figure shows the amplitude of the bound state field at $\kappa = 0$. (c) Results of numerical simulation using boundary integral equations: transmission coefficient vs normalized frequency for TE-polarized plane wave incident on a grating of vertical rods in air for various values of the wave vector y-component. Permittivity of the cylinders is 12, and permeability is 1. (Adapted from [36].)

transmission through an array of parallel dielectric cylinders (Fig. 4b). In the same year, they developed a theory explaining the formation of bound states and anomalies in the transmission spectrum corresponding to these states [36]. Figure 4c shows the numerically obtained transmission spectrum for various Bloch wave numbers. It is shown that, at normal incidence, the Fano resonance collapses. The bottom part of Fig. 4b presents the electric field distribution of the bound state. In fact, it is antisymmetric with respect to the plane of symmetry of the unit cell; however, the authors plotted the distribution amplitude, which is an even function. In 2003, Bonnet et al. [37] discovered an ultranarrow-band resonant reflection from a one-dimensional corrugated waveguide at oblique incidence, i.e., at a nonzero Bloch wave number, and analyzed the effect of a finite beam size on the reflection spectrum.

Probably the first experiment on observing BICs was carried out in 1985 by Henry et al. [39]. They considered a distributed-feedback resonator with a second-order grating and showed that the losses of the lasing mode mainly occur at the ends of the structure, whereas at its center they nearly vanish due to the destructive interference of the scattered radiation from counter-propagating waves forming the lasing mode, as was predicted in Ref. [29]. Later on, in 1986, Avrutskii et al. [40] analyzed the spectra of reflection from a corrugated ZnO waveguide deposited on a glass substrate in the visible range. It was found that a peak in the second stop band disappears from the spectrum at normal incidence, manifesting the bound state formed by counterpropagating guided modes.

Another experiment was carried out by Robertson et al. in 1992 [41]. They analyzed the transmission spectra of a two-dimensional dielectric structure consisting of alumina-ceramic cylinders arranged in a square array. The experiment was performed in the GHz frequency range (10–150 GHz). The authors noted that one of the bands was not observed in the experiment because of the symmetry mismatch between the eigenmode and the exciting field. An experiment on the observation of BICs in the visible range was performed by Pacradouni et al. [42], who measured the reflection spectra with angular resolution from a perforated AlGaAs membrane, confirming the narrowing of lines in the BIC vicinity both at the Γ point (upon normal incidence) and off the Γ point (upon oblique incidence). However, we should note that Ref. [42] contains a minor inaccuracy. The issue is that the existence of BICs with a nonzero Bloch wave vector requires either a mirror symmetry in the structure plane [43] or a very fine adjustment of the geometric and material parameters of the structure [44], which, according to [42], was not performed. Thus, the authors of Ref. [42] observed only an increase in the Q factor, rather than a BIC. To observe an off-Γ BIC, i.e., a BIC with a nonzero Bloch vector, in photonic crystal membranes, the structure is usually either suspended [45] or covered by a liquid whose refractive index matches that of the substrate [46], thus providing mirror symmetry in the structure plane. The at-Γ BICs were also observed experimentally in polariton systems in 1998 by Fujita et al. [47]. They analyzed angular-resolved transmission spectra for a distributed-feedback microcavity consisting of a quartz grating playing the role of a substrate covered by an organic-inorganic perovskite-type semiconductor. They discovered that at normal incidence the resonances disappear. These experimental results were comprehensively described by Yablonskii et al. [48].

Above, we tried to review the key studies of BICs in electromagnetic systems. However, we should note that the

existence of nonradiating states in photonic structures has also been discussed in many other papers (see, e.g., [40, 49–51]. To conclude this historical summary, we would like to mention that the physics of nonradiating states in periodic structures is quite clear, and other earlier studies might exist, where such states were discussed.

3. Bound states in the continuum in dielectric photonic structures

3.1 From quantum mechanics to photonics

To reveal the relation between quantum mechanics and optics, let us consider the example of a 1D quantum well with a translational symmetry along the z-direction. For such a system, we can define the domain of the continuum spectrum as $\tilde{E} = E - \hbar^2 k_z^2/(2m) > 0$ (Fig. 5a). The optical counterpart of this system is a parallel-plate dielectric waveguide. By reducing the Helmholtz equation to the form of the stationary Schrödinger equation (Fig. 5b), one can see that the permittivity $\varepsilon(x)$ can be associated with quantum mechanical potential $U(x)$. The waveguide modes lying under the light line $\omega < ck_z$ represent discrete states, and all the modes with $\omega > ck_z$ form the continuum. Thus, in the system with a translational symmetry or periodicity along a certain direction, BICs will be localized only in the orthogonal directions. The analogy between quantum and optical systems is very illustrative, but it is not complete. The vector structure of electromagnetic fields (polarization) makes the electromagnetic systems more diverse. We should also note that the Helmholtz equation written in the form of the stationary Schrödinger equation (Fig. 5) is a so-called generalized eigenvalue problem, since the required frequency ω is included both in the eigenvalue (right-hand side of the equation) and in the potential. However, if we consider the wave vector k_z to be an eigenvalue, then we obtain a classical eigenvalue problem.

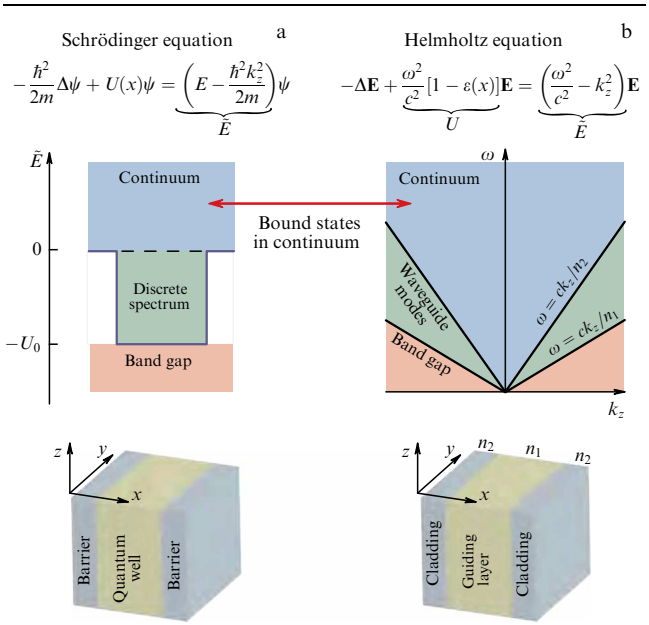

Figure 5. Correspondence between quantum mechanical and electromagnetic problems for a 1D potential having a translational symmetry along the z-axis. (a) Top-down: Schrödinger equation for 1D quantum well, energy spectrum of the potential well and schematic view of the potential well. (b) Top-down: Helmholtz equation for a planar dielectric waveguide, dispersion diagram, and planar waveguide in the coordinate space.

One of the general principles that can explain the appearance of BICs in most electromagnetic systems is the destructive interference of two interacting leaky waves. This mechanism was originally proposed by Friedrich and Wintgen [7], and it is schematically shown in Fig. 6a. Let an open system (resonator) have two leaky modes $|\psi_s\rangle$ $(s = 1, 2)$ with close or even equal eigenfrequencies $\Omega_s = \omega_s + \mathrm{i}\gamma_s$. Let us introduce a perturbation $\hat{V}$ that makes these states coupled. In the framework of the perturbation theory, the eigenmodes in the system, with the interaction taken into account, can be presented as a linear superposition of the initial states $|\psi\rangle = C_1|\psi_1\rangle + C_2|\psi_2\rangle$. If we can continuously vary the interaction potential $\hat{V}$, then, under certain conditions, the radiative losses can be completely (or substantially) suppressed and a genuine BIC (or a quasi-BIC) arises.

From a formal point of view, an open system within the two-mode approximation can be described using the coupled-mode theory in the time domain, where $\mathbf{a} = [a_1(t), a_2(t)]^{\mathrm{T}}$ are the complex amplitudes of states $|\psi_1\rangle$ and $|\psi_2\rangle$. The complex amplitudes evolution in time is described by the equation

$$\frac{\mathrm{d}\mathbf{a}}{\mathrm{d}t} = \hat{H}\mathbf{a}\,, \tag{1}$$

$$\hat{H} = \underbrace{\begin{pmatrix} \omega_1 & \kappa \\ \kappa & \omega_2 \end{pmatrix}}_{\hat{H}_0} - \mathrm{i}\underbrace{\begin{pmatrix} \gamma_1 & \sqrt{\gamma_1\gamma_2}\,\exp(\mathrm{i}\phi) \\ \sqrt{\gamma_1\gamma_2}\,\exp(\mathrm{i}\phi) & \gamma_2 \end{pmatrix}}_{\hat{V}}. \tag{2}$$

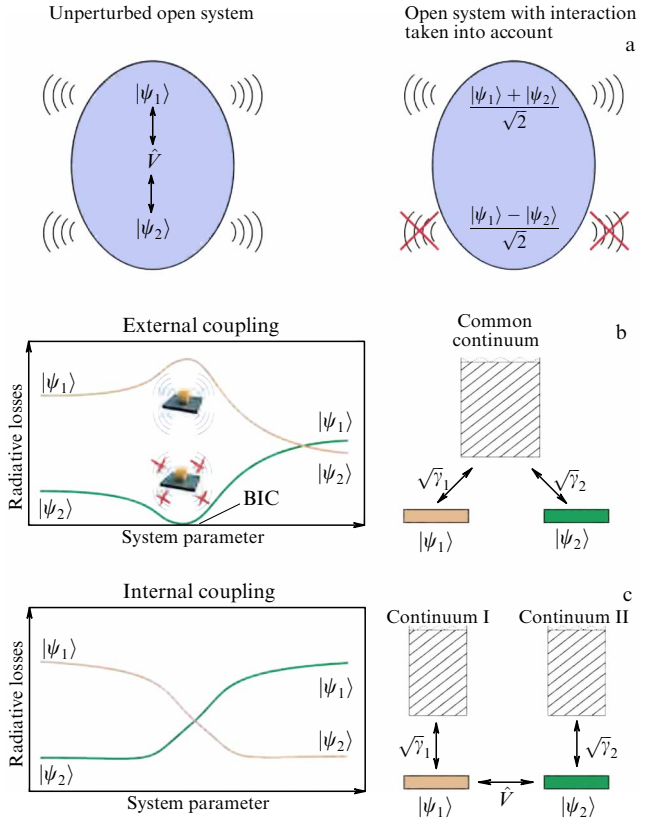

Figure 6. Illustration of the general principle explaining BICs proposed by Friedrich and Wintgen: (a) nonperturbed and perturbed open systems; (b) open system with two interacting leaky modes coupled to the same continuum, which allows for the existence of a BIC; (c) open system with two interacting leaky modes coupled to different radiative continua so that no BIC is allowed.

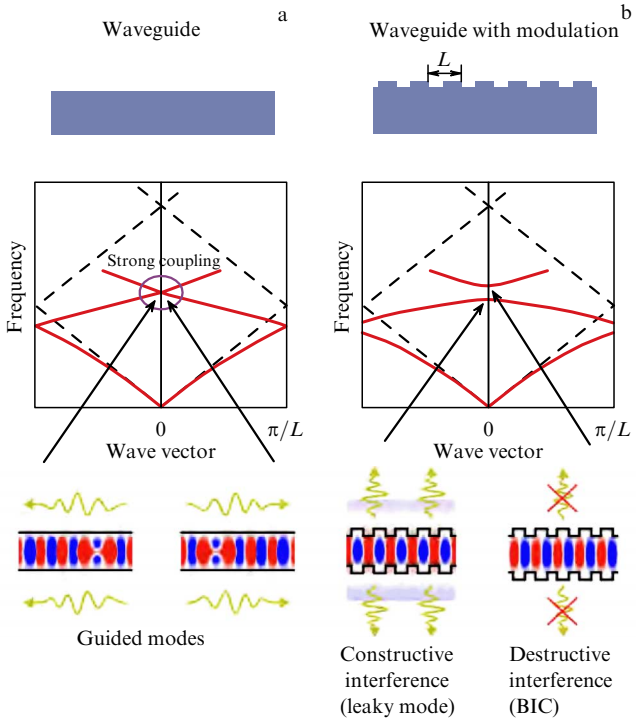

Figure 7. (a) Geometry, folded band diagram, and mode profiles for a planar dielectric waveguide. Waveguide modes can propagate to the left or to the right. (b) Geometry, folded band diagram, and mode profiles for a planar dielectric waveguide modulated with period L. Periodicity gives rise to coupling of waveguide modes, so that two new states appear, namely, a leaky mode and a BIC due to constructive and destructive interference, respectively.

Here, κ is responsible for the internal coupling of modes, $\sqrt{\gamma_1\gamma_2}$ accounts for coupling through the radiation continuum, and ϕ is the phase shift between the modes. The condition of the BIC appearance in the two-mode approximation can be written as [52]

$$\kappa\,(\gamma_1 - \gamma_2) = \exp\,(\mathrm{i}\phi)\,\sqrt{\gamma_1\gamma_2}\,(\omega_1 - \omega_2)\,, \tag{3}$$

$$\phi = \pi m\,, \tag{4}$$

where m is an integer. Conditions (3), (4) can be fulfilled through the tuning of the parameters of two coupled resonances. Figure 6b shows schematically how the radiative losses of the resonant states ψ_1 and ψ_2 depend on the coupling constant κ. Note that, exactly at the point where the BIC appears, the radiative losses for the second mode are exactly equal to $\gamma_1 + \gamma_2$. This is an analog of the Dicke superradiance for two sources [53, 54].

In the framework of this simple model, the initial resonant states should radiate to the same radiative continuum (scattering channel). Only in this case can they interfere destructively and form a BIC. If the states $|\psi_1\rangle$ and $|\psi_2\rangle$ radiate to different continua, then the radiative losses of the 'dressed' states will always be between γ_1 and γ_2 (Fig. 6c) [55].

For more clarity, let us show how this model explains the formation of BICs in a corrugated dielectric waveguide. First, let us consider a periodic potential with amplitude tending to zero (Fig. 7a). This is the so-called 'empty lattice' limit, which is well known in solid state physics [56]. Then, the second bandgap width becomes zero, and the eigenstates at the Γ point are degenerate counterpropagating leaky waves. A periodic potential with finite amplitude removes the degeneracy and opens the bandgap. If the periodic potential is symmetric with respect to the $z \to -z$ transformation, then the new states at the edges of the second bandgap are a BIC (antisymmetric combination of the leaky modes) and a superradiant state (symmetric combination of the leaky modes) (Fig. 7b). This clear mechanism of BIC formation was discussed in many papers, e.g., in [29, 57–59].

3.2 Bound states in the continuum and diffraction orders

A leaky mode can transform into a BIC if the amplitudes of scattering to all the channels turn to zero, i.e., in the case of decoupling from all the open scattering channels, which can be achieved by varying the system parameters. In this case, BIC formation is possible only if the number of adjusted parameters is greater than the number of scattering channels. For finite-size structures, the number of scattering channels is infinite, and the existence of BICs in such systems is prohibited by the appropriate 'nonexistence' theorem [23]. The only exception is structures surrounded by a completely opaque shell providing the decoupling of the internal resonances from the outside radiation continuum. In quantum mechanics, this corresponds to an infinite potential barrier, in acoustics, to hard-wall boundaries, and in optics, to perfectly conducting walls or barriers with the dielectric constant close to zero [60, 61]. Thus, BICs are usually formed in structures with a finite number of scattering channels. A typical example of such a system is a resonator coupled to one or several waveguide modes [20, 62, 63] or infinite photonic structures periodic in one or two directions [21, 43, 46, 64, 65].

Let us consider in more detail the mechanism of BIC formation in periodic structures using the example of a dielectric grating with period L (Fig. 8a). The electric field, being a Bloch function, can be presented in the form

$$\mathbf{E}_{n,k_\mathrm{B}}(x,y,z) = \exp\,(\mathrm{i}k_\mathrm{B}z + \mathrm{i}k_y y)\,\mathbf{u}_{n,k_\mathrm{B}}(x,z)\,. \tag{5}$$

Here, k_B is the Bloch wavenumber, k_y is the wavenumber component along the y-axis (the direction of the translational symmetry), and n is the index of the photonic band. Function $\mathbf{u}_{n,k_\mathrm{B}}(x,z)$ is periodic and can be expanded into the Fourier series

$$\mathbf{u}_{n,k_\mathrm{B}}(x,z) = \sum_s \mathbf{c}_{n,s,k_\mathrm{B}}(x)\,\exp\left(\frac{2\pi\mathrm{i}s}{L}\,z\right), \tag{6}$$

where s is an integer. Each term in series (6) corresponds to a diffraction channel, which could be open or closed. Outside the structure, the expansion coefficients correspond to plane waves:

$$\mathbf{c}_{n,s,k_\mathrm{B}}(x) \to \mathbf{c}_{n,s,k_\mathrm{B}}\exp\,(\pm\mathrm{i}K_s x)\,, \tag{7}$$

$$K_s = \sqrt{\frac{\omega^2}{c^2} - k_y^2 - \left(k_\mathrm{B}^2 + \frac{2\pi s}{L}\right)^2}\,. \tag{8}$$

If K_s is real, then the diffraction channel is open and $\mathbf{c}_{n,s,k_\mathrm{B}}$ is the complex amplitude of the wave outgoing via the sth diffraction channel. If K_s is imaginary, then the diffraction channel is closed, and $\mathbf{c}_{n,s,k_\mathrm{B}}$ is the complex amplitude of the near field.

Figure 8b shows schematically the typical dispersion (dependence of ω on k_B for $k_y = 0$) for the eigenmodes in a dielectric grating. The colored areas correspond to the regions where a certain number (N) of diffraction channels are open. Under the light line, $N = 0$. Therefore, all the diffraction

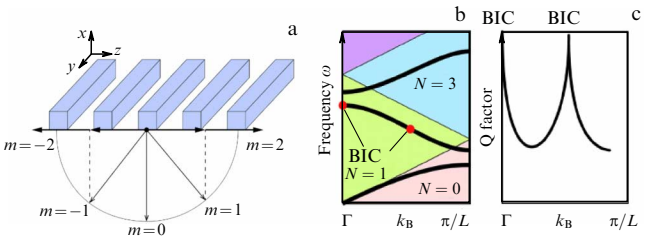

Figure 8. (a) Example of a 1D dielectric grating. (b) Typical dispersion diagram, where colors indicate domains with different numbers of open diffraction channels, and red circles indicate positions of BICs. (c) Variation of the Q factor along the second dispersion curve.

channels are closed, and only the waveguide modes exist in the structure.

To form a BIC, all the coefficients $\mathbf{c}_{n,s,k_B}$ corresponding to the open diffraction channels should be equal to zero. However, for subwavelength structures with $L < \lambda$, there is only one open diffraction channel ($N = 1$) corresponding to $s = 0$. Therefore, in order to form a BIC, we need to nullify $\mathbf{c}_{0,k_B}(x)$. Hereinafter, we omit the index n for the sake of simplicity. The function $\mathbf{c}_{0,k_B}(x)$ is the zeroth Fourier coefficient in expansion (6). Then, according to the definition,

$$\mathbf{c}_{0,k_B}(x) = \int_{-L/2}^{L/2} \mathbf{u}_{k_B}(x,z)\,\mathrm{d}z\,. \tag{9}$$

For the state in the center of the Brillouin zone ($k_B = 0$), one can write

$$\mathbf{c}_{0,0}(x) = \int_{-L/2}^{L/2} \mathbf{u}_{0,0}(x,z)\,\mathrm{d}z = \left\langle \mathbf{u}_{0,0}(x,z)\right\rangle_z. \tag{10}$$

Therefore, for a BIC at the Γ point, the z-averaged field should be equal to zero. If the unit cell of the grating is symmetric with respect to the $z \to -z$ transformation, then the eigenstates in the Γ point can be even or odd functions of z. For odd functions, their z-averaged value is zero. Therefore, all such states are BICs. These BICs are called symmetry protected, which means that the suppression of radiation is protected by the symmetry of the structure. Therefore, symmetry-protected BICs can emerge in both low-contrast and high-contrast photonic structures [59, 66, 67]. As opposed to symmetry-protected BICs, there are accidental BICs (also referred to as Friedrich–Wintgen BICs), in which $\mathbf{c}_{0,k_B}(x)$ turns into zero not because of the symmetry, but due to the tuning of the system parameters [43, 46].

In the general case, the Fourier amplitude $\mathbf{c}_{0,k_B}$ is a complex vector function of the grating parameters. Therefore, for BIC formation, both its real and imaginary parts should be zero. However, one can show that, for BICs, the components of $\mathbf{c}_{0,k_B}$ can be real everywhere in the $\mathbf{k}$-space, if the structure possesses time-reversal symmetry $\varepsilon^*(\mathbf{r}) = \varepsilon(\mathbf{r})$, inversion symmetry $\varepsilon(-\mathbf{r}) = \varepsilon(\mathbf{r})$, and mirror symmetry with respect to the structure plane [43, 46]. In the case of symmetry-protected BICs, the last condition is unnecessary, so that they can be implemented in structures with a substrate. However, to observe accidental (off-Γ) BICs, this symmetry is necessary. Therefore, as was mentioned above, in experiments, the samples are usually immersed in a liquid that is index-matched to the substrate, or suspended structures are used [46, 68].

To form a BIC, it is not necessary to work in a region with only one diffraction channel open. If several diffraction channels are open, one has to tune a number of parameters of the system, which is hard to implement in practice, but there are theoretical studies showing that it is possible [69, 70].

3.3 Bound states in the continuum and multipole expansion

The appearance of BICs in periodic photonic structures can be explained in terms of the multipole expansion method. Multipole expansion is based on the formalism of the vector spherical harmonics (multipoles) representing a complete basis set of orthogonal vector functions that are solutions of the vector Helmholtz equation [71]. Usually, these functions, used in the Mie theory to describe independent scattering channels, make it possible to relate the directional pattern of the outgoing radiation and the polarization currents induced inside a scatterer by the incident wave [72]. Using the multipole expansion, a number of phenomena in the area of electromagnetic waves scattering were explained, including the anapole states [73, 74], the Kerker effect [75–77], and superscattering [78–81]. The multipole approach can also enable a deeper understanding of the physics of BICs in periodic structures.

Following the book by Bohren and Huffman [82], we define the vector spherical harmonics $\mathbf{M}_{p\ell m}$ and $\mathbf{N}_{p\ell m}$ as

$$\mathbf{M}_{p\ell m} = \nabla \times (\mathbf{r}\psi_{p\ell m})\,,\ p = \mathrm{o}\,(\mathrm{odd}), \mathrm{e}\,(\mathrm{even})\,, \tag{11}$$

$$\mathbf{N}_{p\ell m} = \frac{1}{k}\nabla \times \nabla \times (\mathbf{r}\psi_{p\ell m})\,,\quad p = \mathrm{o}, \mathrm{e}\,, \tag{12}$$

$$\psi \left\{ \begin{matrix} \mathrm{e} \\ \mathrm{o} \end{matrix} \right\}_{\ell m} = z_\ell\,(kr) P_\ell^m\,(\cos\theta) \left\{ \begin{matrix} \cos\,(m\varphi) \\ \sin\,(m\varphi) \end{matrix} \right\}. \tag{13}$$

Here, $\{r, \theta, \varphi\}$ are spherical coordinates, P_ℓ^m is an associated Legendre polynomial, $z_\ell(kr)$ is a spherical Bessel function describing the incoming, outgoing, or standing wave, $\ell = 1, 2, 3, \ldots$ is the total angular momentum, $m = 0, 1, \ldots, \ell$ is the absolute value of the projection of the angular momentum (magnetic quantum number), and k is the wavenumber in a vacuum or medium depending on the considered domain of the space. For brevity, we introduce $\mathbf{W}_j = \{\mathbf{M}_{p\ell m}, \mathbf{N}_{p\ell m}\}$, where $j = \{p, \ell, m\}$. Let us consider an eigenmode of a photonic crystal waveguide or a metasurface (Fig. 9a). The electric field of the mode outside the structure can be represented as

$$\mathbf{E}\,(\mathbf{r}) = \sum_{\mathbf{K}_s, j} D_j \int\!\!\int_{-\infty}^{+\infty} \mathrm{d}\mathbf{k}_\parallel \frac{\exp\,(\mathrm{i}\mathbf{k}\mathbf{r})}{k_z}\, \mathbf{Y}_j \left(\frac{\mathbf{k}}{|\mathbf{k}|}\right) \delta\,(\mathbf{k}_B - \mathbf{K}_s - \mathbf{k}_\parallel)\,. \tag{14}$$

Here, $\mathbf{Y}_j$ is the Fourier transform of $\mathbf{W}_j$, $\mathbf{k}_B$ is the Bloch wave vector, $\mathbf{K}_s$ is the reciprocal lattice vector, D_j is the amplitude corresponding to $\mathbf{Y}_j$. The coefficient D_j of the far field expansion is directly related to the coefficient of the polarization expansion in vector spherical harmonics inside the unit cell [83].

Expression (14) shows that the far field of the structure is defined not only by the multipole content of the unit cell but also by the open diffraction channels. The BICs are formed under the condition that the directions of all the open diffraction channels coincide with the nodal lines of the unit cell field.

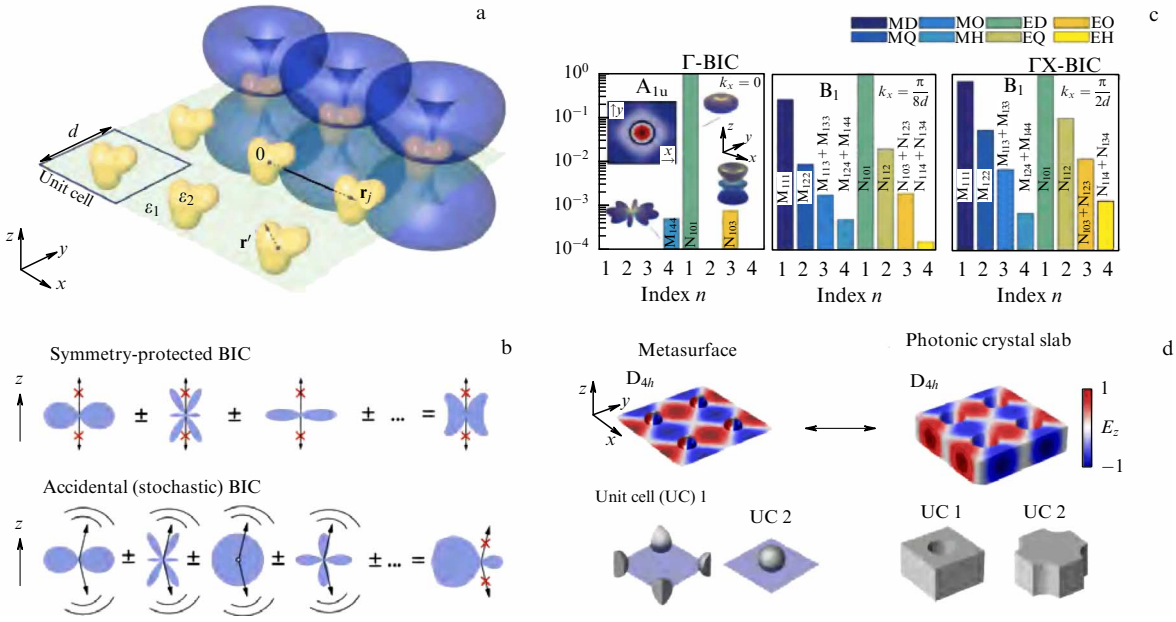

Figure 9. Illustration of BIC formation mechanism in terms of multipoles. (a) Periodic dielectric metasurface with a square lattice. (b) Mechanism of BIC formation. (c) Multipole expansion of the TM-polarized eigenmode of the metasurface composed of dielectric spheres with $\varepsilon_2 = 12$ ($\varepsilon_1 = 1$). Each of the images corresponds to a fixed Bloch wavenumber k_x. Vertical axis shows the relative amplitude of electric and magnetic multipoles; different orders n are shown in different colors. A_{1u} and B_1 are irreducible representations. Inset at the top of the figure demonstrates the E_z field profile in the central cross section. (d) Distribution of the E_z component of the electric field of modes corresponding to the same irreducible representation B_{1u} in the photonic crystal slab or metasurface. Bottom panel illustrates examples of unit cells with similar multipole content. (Adapted from [83].)

The simplest example is the subwavelength lattice of identical in-phase point dipoles oriented perpendicular to the lattice plane. Such a configuration corresponds to the mode with $\mathbf{k}_B = 0$, i.e., to the Γ point of the reciprocal space. The only allowed direction of the diffraction is normal to the metasurface; however, dipoles do not radiate in the direction of their axis. Therefore, this mode is nonradiative and represents a symmetry-protected BIC [84]. It is shown in Ref. [83] that there are two scenarios of the appearance of BICs in subwavelength structures (Fig. 9b). In the first case, none of the multipoles contributing to the eigenmode radiate in the direction orthogonal to the structure. This corresponds to symmetry-protected BICs. It can be shown that the multipoles $\mathbf{M}_{p\ell m}$ and $\mathbf{N}_{p\ell m}$ do not radiate upward or downward if $m \neq 1$ [83]. Thus, all the modes at the Γ point not containing multipoles with $m = 1$ are symmetry-protected BICs. In the second case, the interference of all the multipoles entering into the composition of the mode suppresses radiation in the direction of the open diffraction channel. This corresponds to accidental BICs.

To find all the multipoles that can enter into the composition of a certain mode, the group theory can be addressed. The eigenmodes are transformed by irreducible representations of the symmetry group of the structure [85–87]. In this case, the unit cell determines the point group symmetry and the Bloch functions form a basis of irreducible representation of the translation group. The symmetry group of a particular wave vector $\mathbf{k}_B$ is defined as a subgroup of the whole point group that keeps $\mathbf{k}_B$ invariant. Thus, to determine the multipole composition of the mode, we should first find the irreducible representation of the mode for the given $\mathbf{k}_B$. The set of multipoles in the decomposition is determined directly by the irreducible representation of the mode. Figure 9c shows the multipole composition of the mode supported by an array of dielectric spheres with a square unit cell. The parameters of the structure are indicated in the figure caption. At the Γ point, the $\mathbf{k}_B$ group coincides with the symmetry point group of the unit cell. Out of the Γ point, the irreducible representation changes. The left part of Fig. 9c shows three main multipoles contributing to the symmetry-protected BIC in the considered example. As was mentioned above, for accidental BICs, the sum of the vector spherical harmonics Eqn (14) is zero in the direction of the open diffraction channel. The multipole composition of the tunable BIC is shown in the right part of Fig. 9c.

It can be shown that in a square lattice (D_{4h}, C_{4v}) all singlet states at the Γ point with the frequency $\omega < 2\pi c/d$ are symmetry-protected BICs, whereas the bright modes are doubly degenerate [83]. However, in a triangular lattice (D_{6h}, C_{6v}), there are two two-dimensional representations. One of them does not contain multipoles with $m = 1$. Therefore, such structures can host doubly-degenerate symmetry-protected BICs [88]. Recently, Overvig et al [89] presented a detailed set of the selection rules for symmetry-protected BICs in two-dimensional photonic crystal structures.

If a metasurface consists of meta-atoms characterized by a single multipole (dipole, quadrupole, octupole, etc.), then the position of the accidental BIC in the k-space is determined by the direction of the nodal line of the multipole. Of course, the multipole approach is natural for metasurfaces consisting of resonant meta-atoms, but, generally speaking, it can also be applied to photonic crystal structures in the case of low-contrast materials or when the filling factor is low. For example, Fig. 9d shows the field distribution for two modes of similar symmetry in a metasurface and a photonic crystal slab with D_{4h} symmetry.

3.4 Bound states in the continuum and topological charges

Usually, BICs are robust to a change of some parameters of the system — they shift in the configuration space, rather than

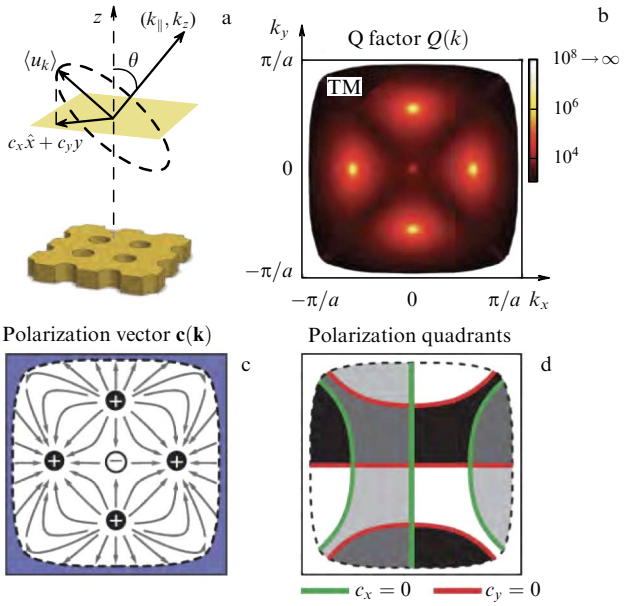

Figure 10. (a) Schematic diagram of the expansion of the radiation field for resonances of a photonic crystal slab. Spatially-averaged Bloch part of the electric field $\mathbf{c}(\mathbf{k}) = \langle \mathbf{u}_\mathbf{k} \rangle$ is projected onto the xy plane as the polarization vector $\mathbf{c}(\mathbf{k}) = (c_x, c_y)$. Resonance turns into a BIC when $c_x = 0$ and $c_y = 0$. (b) Map of the radiative Q factor calculated for TM_1 modes of a square-lattice photonic crystal slab in the first Brillouin zone. For the plotted mode, five BICs are visible: four accidental and one symmetry protected. (c) Directions of vector field polarization show the vortices with topological charges ± 1. Blue shading indicates the region below the light line. (d) Nodal lines of the components of the polarization vector $\mathbf{c}(\mathbf{k})$. (Adapted from [43].)

disappear. Such robustness may have a topological origin and, thus, can be characterized by topological invariants (topological charges). In this section, we consider three illustrative examples of topological robustness of BICs in the configuration space. As we have shown in Section 3.3, BICs appear in periodic structures when the vector Fourier amplitude corresponding to the radiation to the open diffraction channel becomes zero. It was demonstrated in Ref. [43] that the polarization structure of the Fourier amplitude in the vicinity of a BIC forms a vortex that can be characterized by a topological charge showing the number of 2π rotations of the polarization vector while going around the BIC point in the reciprocal space.

According to the Bloch theorem, the electric field of a mode in a photonic crystal waveguide (Fig. 10a) can be written (by analogy with the case of 1D grating considered above) as

$$\mathbf{E}_\mathbf{k}(\boldsymbol{\rho}, z) = \exp(\mathrm{i}\mathbf{k}\boldsymbol{\rho})\, \mathbf{u}_\mathbf{k}(\boldsymbol{\rho}, z)\,. \tag{15}$$

Here, $\mathbf{k} = (k_x, k_y, 0)$ is the two-dimensional Bloch wave vector, $\boldsymbol{\rho} = (x, y, 0)$ is the radius vector lying in the plane of the structure, and z is the coordinate directed normally to the waveguide. Function $\mathbf{u}_\mathbf{k}(\boldsymbol{\rho}, z)$ is periodic in $\boldsymbol{\rho}$. The zero-order Fourier amplitude $\mathbf{c}(\mathbf{k}) = \langle \mathbf{u}_\mathbf{k} \rangle$ determines the amplitude and polarization of the outgoing wave. The spatial average is taken over the unit cell in any horizontal plane outside the waveguide. Since the BIC radiates neither x nor y polarization, it appears in $\mathbf{k}$-space at the crossings of the lines corresponding to $c_x(k_x, k_y) = 0$ and $c_y(k_x, k_y) = 0$ (Fig. 10b, d). The topological charge q characterizing the BIC can be introduced as

$$q = \frac{1}{2\pi} \oint_\mathrm{C} \mathrm{d}\mathbf{k}\, \nabla_\mathbf{k} \phi(\mathbf{k}), \quad q \in \mathbb{Z}. \tag{16}$$

Here, $\phi(\mathbf{k}) = \arg(c_x(\mathbf{k}) + \mathrm{i}c_y(\mathbf{k}))$, and C is a path in $\mathbf{k}$-space that goes around the BIC in the counter-clockwise direction. The polarization vector has to come back to itself after passing the closed loop, so the overall angle change must be an integer multiple of 2π, and, thus, q must be an integer. For the considered structure, the symmetry-protected BIC has a charge of $q = 1$ (Fig. 10c). The topological charge of the BIC hosted by the silicon nitride grating was measured experimentally using angle- and wavelength-resolved polarimetric reflectometry [90]. It was shown in Ref. [43] that the topological charge of BICs in one-dimensional gratings can take only the values $q = 0, \pm 1$. The topological charge in structures periodic in two dimensions can be arbitrarily large. However, in all known photonic structures proposed to date, the maximum value of the BIC topological charge amounts to $|q| = 2$ [43, 91]. The observation of a BIC with a higher topological charge is a complex problem not yet solved.

Being robust against changes in some geometrical parameters of the structures, the polarization vortex can migrate over the dispersion surface within the Brillouin zone. For a particular photonic branch, the total topological charge is conserved, which imposes restrictions on the behavior of BICs. For example, a BIC can be destroyed through annihilation when two or several topological charges with total zero charge collide. A BIC with an integer topological charge can decay into several BICs with integer topological charges or into circularly polarized states with half-integer charges [43, 91, 94, 95]. Some examples of the topological charge migration and decay will be considered in Section 4.1. The topological charge carried by a BIC can be used to generate optical vortex beams [96–98].

In Ref. [92], a general approach for determining the topological charge of a BIC in a wide class of systems is developed and applied to linear periodic chains of coupled resonators (Fig. 11a). The authors of Ref. [92] introduced a complex function $W(\omega, k_z)$ (quasimode coupling strength) characterizing the efficiency of coupling between the scattering channel and the resonant states of the system. Here, k_z is the wavenumber of the incident wave with frequency ω. Function $W(\omega, k_z)$ can be considered a projection of the incident wave onto the eigenmode or the projection of the resonant state onto the wave outgoing through the scattering channel which is the same thing. Obviously, $W(\omega, k_z) = 0$ for the BIC, because the BIC arises in the $\omega - k_z$ space exactly at the crossing of lines corresponding to $\mathrm{Re}\, W(\omega, k_z) = f(\omega, k_z) = 0$ and $\mathrm{Im}\, W(\omega, k_z) = g(\omega, k_z) = 0$. Then, the topological charge q can be introduced as

$$q = \mathrm{sgn}\left(\frac{\partial f}{\partial \omega} \frac{\partial g}{\partial k_z} - \frac{\partial g}{\partial \omega} \frac{\partial f}{\partial k_z} \right)\Bigg|_\mathrm{BIC}. \tag{17}$$

Figure 11b shows the phase $\theta = \arg W(\omega, k_z)$. One can see that the gradient of the phase $\mathbf{j} = \nabla\theta$ forms a vortex around the BIC. Therefore, a BIC in a linear periodic chain can also be characterized by a topological charge. However, it is still an open question as to how to measure such a charge experimentally.

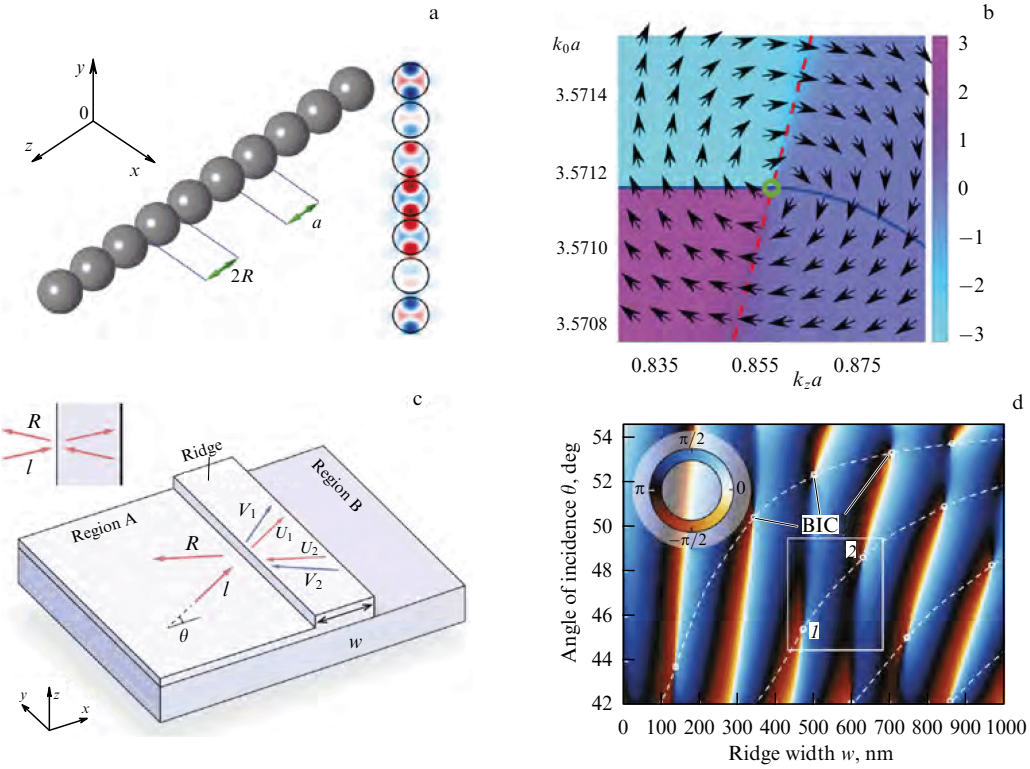

Figure 11. (a) Periodic array of dielectric spheres and BIC magnetic field amplitude H_z in the yz plane. (b) Phase of coupling coefficient $W(\omega, k_z)$. Arrows demonstrate the presence of a vortex near the BIC. (Adapted from [92].) (c) Schematic view of the on-chip analog of the Gires–Tournois interferometer, in which the appearance of a BIC is possible. (d) Phase of the coupling coefficient $\mathcal{P}(w, \theta)$. (Adapted from [93].)

Another elegant example of a BIC was observed in the dielectric ridged waveguide forming an on-chip analog of the Gires–Tournois interferometer (Fig. 11c) [93]. The authors of [93] showed that such a waveguide can support a BIC — the mode that couples neither to waveguide modes in region A nor to the propagating waves in the substrate and in free space. This type of BIC was predicted and experimentally observed in Refs [99–101]. A rigorous theory proving that these states are BICs was developed by Bezus, Bykov, and Doskolovich [102]. By analogy with Ref. [92], the authors of [102] introduced a complex quasimode coupling $\mathcal{P}(w, \theta)$ between the modes of the ridge and waveguide modes in region A. If the frequency is fixed, then the BIC in the considered system can be observed at specific values of angle θ and ridge width w. Exactly at the BIC, the function $\mathcal{P}(w, \theta)|_{\text{BIC}} = 0$, and its phase is singular (i.e., indefinite). The topological charge introduced as

$$q = \frac{1}{2\pi} \oint_{\gamma} \mathrm{d} \arg \mathcal{P}(w, \theta) \tag{18}$$

can be equal to ± 1. By variation of the guiding layer thickness in region B, the authors of Ref. [102] showed that BICs can move in $w-\theta$ space and even annihilate, if two BICs with opposite charges collide (Fig. 11d). We should note that, instead of varying the ridge width w at a fixed frequency ω, one can vary ω at a fixed ridge width w: the result will be completely the same. To conclude, we should add that the topological charge can be introduced in many ways, but not all of the introduced charges will have a clear physical meaning, and therefore they cannot be measured.

3.5 Losses and the Q factor of quasi-bound states in the continuum

Losses limit the total Q factor Q_{tot} of a BIC. In general, Q_{tot} can be decomposed into partial contributions:

$$Q_{\text{tot}}^{-1} = \underbrace{Q_{\text{rad}}^{-1} + Q_{\text{surf}}^{-1} + Q_{\text{str}}^{-1} + Q_{\text{size}}^{-1} + Q_{\text{subs}}^{-1}}_{\text{radiative}} + \underbrace{Q_{\text{abs}}^{-1}}_{\text{nonradiative}} . \tag{19}$$

In Eqn (19), in addition to the radiative part Q_{rad} proper, the radiative losses allow for surface roughness (Q_{surf}), structural disorder (Q_{str}), diffraction losses due to finite size of the sample (Q_{size}), and diffraction into a high-index substrate (Q_{subs}). The nonradiative losses Q_{abs} include all types of absorption (fundamental absorption, free-carrier absorption, multiphoton absorption, etc). The loss mechanisms in periodic photonic structures are shown schematically in Fig. 12a. However, the statement that BICs have a infinite Q factor, quite common in the literature, is not correct. When the BIC is completely decoupled from the radiative continuum, only the radiative Q factor diverges ($Q_{\text{rad}} \to \infty$), but the total Q factor can remain finite. For example, BICs with finite Q_{tot} can be observed in plasmonic structures, where the level of losses is rather high [103–105].

Strictly speaking, BICs are a mathematical idealization, and unavoidable radiative losses turn them into *quasi-BICs*, which manifest themselves in the scattering spectra as narrow Fano resonances [106]. Quasi-BICs are important from a practical point of view, as they are still strongly localized and provide a significant enhancement of the incident field; in addition, they can be excited by an external incident wave. Usually, the efficient performance of photonic structures requires a critical coupling of the eigenmode to the incident

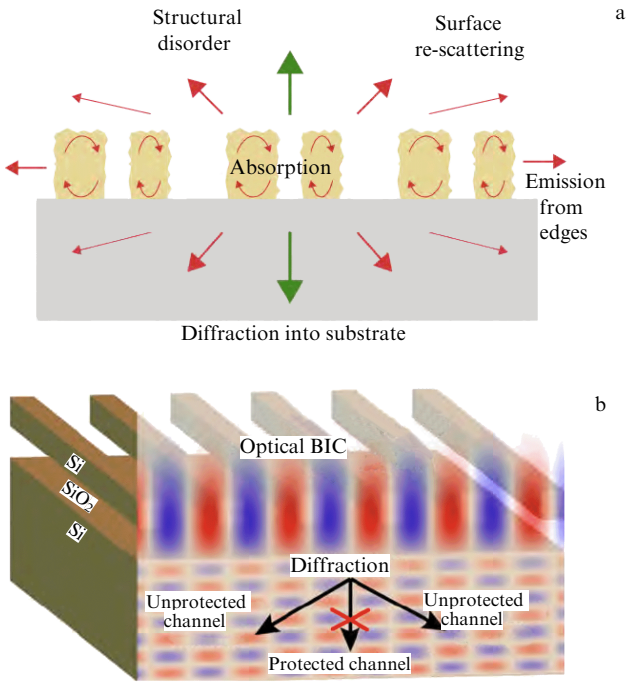

Figure 12. (a) Mechanisms of losses in periodic photonic structures, including scattering by surface roughness, scattering due to structural disorder, diffraction losses due to finite size of the sample, and diffraction into a high-index substrate. (b) Symmetry-protected BIC in a grating etched on a silicon-on-insulator wafer. Diffracted radiation propagating normal to the surface is prohibited by the symmetry of the BIC, whereas diffraction into the substrate is allowed.

field, which is achieved under the condition $Q_{abs} = Q_{rad}$ [107–111]. For example, the absorption rate in semiconductors can be controlled in the visible, infrared, and terahertz ranges via free electrons induced by an external optical pulse [112–114]. The radiative losses of quasi-BICs in periodic photonic structures can be controlled by changing the size of the sample [64, 115, 116], angle of incidence [46], or asymmetry of the unit cell [106]. The last method seems to be the most precise and suitable for practical application to systems excited at normal incidence. The optical properties of photonic structures with quasi-BICs and their applications are discussed in Sections 4 and 5. Another mechanism of dynamic all-optical control over the radiative losses of BICs was proposed in Ref. [117]. It was shown that Kerr nonlinearity can result in radiative losses, which appear due to the coupling between a symmetry-protected BIC and a bright mode of the system, in which case the radiative losses of BICs can be controlled by changing the intensity of the incident light. A similar mechanism of radiative loss control was also proposed for the implementation of optical memory based on BICs [118,119]. One of the loss mechanisms is the diffraction into the substrate with a high refractive index. This mechanism is crucial, for example, for photonic structures fabricated from a silicon-on-insulator wafer [120], where the refractive index of the substrate is higher than the effective refractive index of the BIC and, therefore, a diffraction into the substrate occurs (Fig. 12b). It is important that, despite the presence of a substrate with a high refractive index, zero-order diffraction into the substrate is closed for symmetry-protected BICs, as the substrate does not break C_2 symmetry with respect to the vertical axis. The intensity of the diffraction into the substrate strongly (exponentially) depends on the thickness of the SiO_2 buffer layer that isolates the photonic structure from the substrate. Thus, Q_{tot} increases with the thickness of SiO_2 exponentially until reaching saturation. The saturation plateau is defined by other loss mechanisms. Therefore, the higher the quality of fabrication, the thicker the layer of SiO_2 required.

The radiative loss of BICs in periodic structures is suppressed due to collective destructive interference from all the unit cells of the structure. Therefore, quasi-BICs in the experimental structures have radiative losses that depend on the number of periods N (unit cells) [64, 121–124]. The asymptotic behavior of such losses (Q_{size}) for large N can be estimated from the known dependence of radiative losses in the infinite structure on the Bloch wavenumber, i.e., $Q_{rad} = Q_{rad}(\mathbf{k}_B)$. The transition from the infinite structure, which can be easily analyzed numerically or even analytically, to a finite one is based on the Fabry–Perot quantization of the Bloch wavenumber. Thus, for an in-Γ BIC, Q_{size} is approximately equal to $Q_{rad}(|\mathbf{k}_{B,min}|)$, where $|\mathbf{k}_{B,min}| \approx \pi/L$, and L is the linear size of the structure. Such an approximation has proven to be useful for linear chains [64, 125]. Nevertheless, one should keep in mind that, in some cases, the eigenmodes in an infinite lattice can substantially differ from those in finite structures, even if their size is large [126]. Practically, the width of high-Q Fano resonances ceases to depend on the sample size if it exceeds a few hundred periods. However, recently a configuration was proposed that consists of 27×27 silicon blocks of a dielectric structure hosting a quasi-BIC with experimentally measured $Q_{tot} = 18{,}500$ in the telecommunication frequency range [115]. However, there is no clear recipe for how to fabricate high-Q metasurfaces with a small footprint, and today it remains a highly relevant challenge.

The total Q factor of BICs in periodic dielectric structures in the visible and near-IR ranges is about 10^3–10^4 [46, 64, 88, 116, 125, 127, 128] and it highly depends on the fabrication quality. The radiative Q factor can reach values of 10^6–10^7 [46]. Recently, a symmetry-protected BIC in a photonic crystal slab with a total Q factor of about 10^6 was demonstrated experimentally [129]. The radiation from the edges of the structure was suppressed by surrounding the sample with a photonic crystal with a different lattice constant. In this case, the frequency of the BIC found itself in the bandgap of the surrounding photonic crystal.

Another source of radiative losses is the radiation induced by fabrication defects or structural disorder. Such losses are a common problem for high-Q photonic structures [130–132]. Structural fluctuations are much more difficult to control than, for instance, the sample size. For this reason, the radiation losses due to structural fluctuation and fabrication imperfections usually determine the main loss mechanism limiting the Q factor of BICs. It is known that the structural disorder in periodic photonic structures drastically affects their optical properties, resulting in nontrivial Fano resonance evolution, light localization, coherent back-scattering, etc. [133–137]. The disorder effects are most essential in self-assembled and natural photonic structures [138–140].

According to the generalized theory, the Q factor of a BIC due to structural fluctuations can be presented as $Q_{str}^{-1} \propto \sigma^2$, where σ is the disorder amplitude [141]. Reference [142] analyzes the radiative losses of symmetry-protected BICs in dielectric gratings using the coupled-mode theory, finite element methods, and the supercell formalism. It is shown that radiation is mainly induced by fractional-order Bloch waves, particularly near the zero-order diffraction channel.

Thus, we can say that fluctuations result in BIC rescattering to the neighboring (in **k**-space) states that are leaky. It is noted that, when the size of the unit cell becomes sufficiently large, the influence of the boundary conditions becomes vanishingly small. This can be explained by the spatial localization of the mode, but the authors of [142] did not analyze this effect. The spatial localization of the BICs was demonstrated numerically in Ref. [143], where a one-dimensional periodic structure composed of two layers of dielectric wires was considered. In the same paper, the effect of uncorrelated structural disorder was analyzed for both symmetry-protected and accidental BICs. It was shown that the symmetry-protected BICs are more resistant to the fluctuation of the wire positions in the direction perpendicular to the layers than to fluctuation of the wire position along the layers, and, vice versa, the accidental BICs are more robust against fluctuation along the direction of periodicity. The Anderson localization effect in structures with BICs was discussed in Ref. [144], where a structure similar to that considered by Plotnik et al. (Fig. 2c) [28] was considered. The authors of [144] thoroughly analyzed the stability of the BIC against disorder and showed that, due to the nontrivial interplay between the BIC and disorder-induced localized states, the entanglement of a biphoton survives after averaging over all the disorder configurations.

The authors of Ref. [45] proposed an idea of how to increase the resistance of BICs to structural disorder. They experimentally demonstrated a BIC with a total Q factor of about 5×10^5. The main idea is to merge several BICs in the k-space in the vicinity of the Γ point. Later, the merged BICs, or super-BICs, in photonic crystal slabs were used to achieve a record-low lasing threshold [116]. As we mentioned above, the radiation from BICs due to structural disorder occurs via fractional-order Bloch waves near the Γ point. Thus, in the proposed system, the rescattering takes place mainly between the extremely high-Q states, making the BIC immune against structural disorder.

4. Bound states in the continuum in photonic structures of various dimensions

4.1 Dielectric gratings

In this section, we will consider BICs in 1D dielectric gratings — photonic structures of finite thickness periodic in one direction and having a translational symmetry in the other direction. The study of such structures has a long history, which began in 1887 from Lord Rayleigh's work [145]. Waveguide gratings have been intensively studied since the middle of the 20th century, and they have found numerous applications in distributed-feedback lasers, laser mirrors, bandpass filters, wavelength demultiplexers, polarizers, chemical and bio-sensors, and many other optic and optoelectronic systems. The interested reader may consult reviews [146–150]. Pronounced progress in the physics of optical gratings was related to the development of nanotechnologies, namely, photonic crystals, metasurfaces, flat optics, and high-contrast gratings [151].

Due to simple geometry, BICs in dielectric gratings can be described easily using the Fourier modes method (FMM), also referred to as the rigorous coupled-wave analysis (RCWA) [152] or the true modes method (TMM) [153] specially designed for a high-efficiency description of gratings, as well as resonant state expansion [154, 155], guided mode expansion [156], multiple scattering theory (Korringa–Kohn–Rostoker method) [157], and other methods. The FMM and TMM supplemented with the S-matrix technique provide a powerful tool for analyzing complex multilayer and photonic crystal structures [50, 158].

Along with the symmetry-protected BICs discussed above, the gratings allow implementing another type of BIC, usually called a Fabry–Perot BIC. It is well known that, in the vicinity of optical resonances of nonabsorbing gratings, the transmission coefficient becomes zero (Fig. 4b) [36], i.e., the structure behaves as a perfect mirror. Using two such structures separated by a suitable distance, one can completely trap the light between the gratings. This was the mechanism of BIC formation analyzed in Ref. [21] (Fig. 2a). The Fabry–Perot BIC is a particular case of a tunable (Friedrich–Wintgen) BIC, and it also can be described within coupled-mode theory by Eqns (1) and (2), assuming that $\omega_1 = \omega_2$ and $\gamma_1 = \gamma_2$. Fabry–Perot BICs can appear at both normal $\mathbf{k}_B = 0$ and oblique incidence, when $\mathbf{k}_B \neq 0$.

Actually, there is no need to use a double-layer structure to obtain a Fabry–Perot BIC. It can also appear in gratings with varying thickness, which is described well by modal methods developed in Refs [159–162]. Within these approaches, Bloch modes are used that are propagating eigenmodes of an infinitely thick grating, similar to plane waves in free space [161]. A plane interface between a homogeneous medium and a photonic crystal couples the modes to each other (upon reflection) and to plane waves of the surrounding space or substrate (upon transmission), as illustrated in Fig. 13a. As the slab is bounded by two interfaces, multiple Fabry–Perot-like resonances appear in the reflection spectra (Fig. 13b). In this case, the linewidth of the resonances strongly depends on the thickness of the grating t_g, and at particular values of t_g, the resonances disappear from the spectra (collapse), turning into BICs. The formation of Fabry–Perot BICs requires the presence of at least two Bloch modes in the spectrum of the infinitely thick grating. Indeed, as one can see from Fig. 13b, regardless of the slab thickness, BICs can exist only for $\lambda < \lambda_{c2}$. This condition defines the cutoff frequency of the second-order Bloch mode. This approach was used by Ovcharenko et al. [163], who applied the multimode Fabry–Perot model developed by Tishchenko [161] and Lalanne [159] and showed that this model predicts the existence of BICs and their positions in the parameter space with high accuracy. Using the same formalism, Bykov et al. [164] obtained a simple closed-form expression describing BIC positions in the dispersion diagram. Similar results were obtained by Parriaux and Lyndin [165], but without any reference to BICs.

A further description of BICs in 1D gratings is possible in terms of the scattering matrix (S-matrix) poles [50, 166–168]. The collapse of the Fano resonance for BICs means the merging of the S-matrix zeros and poles [169]. This condition can be used to find the particular parameters at which the BIC appears [93]. Blanchard et al. [170] proposed a phenomenological approach based on the S-matrix pole-zero approximation to describe Fano resonances in the vicinity of BICs. Combining the pole and coupled-wave formalisms for waveguide resonances of a grating was carried out by Pietroy et al. [171]. The authors of [37] explained the ultra-narrow resonance corresponding to an accidental BIC by the strong coupling between the guided modes. By means of expansion in resonant states, using the analytically known modes of planar waveguides as a basis, one can describe the entire diversity of resonances in a photonic crystal slab [155], in particular, BICs [172].

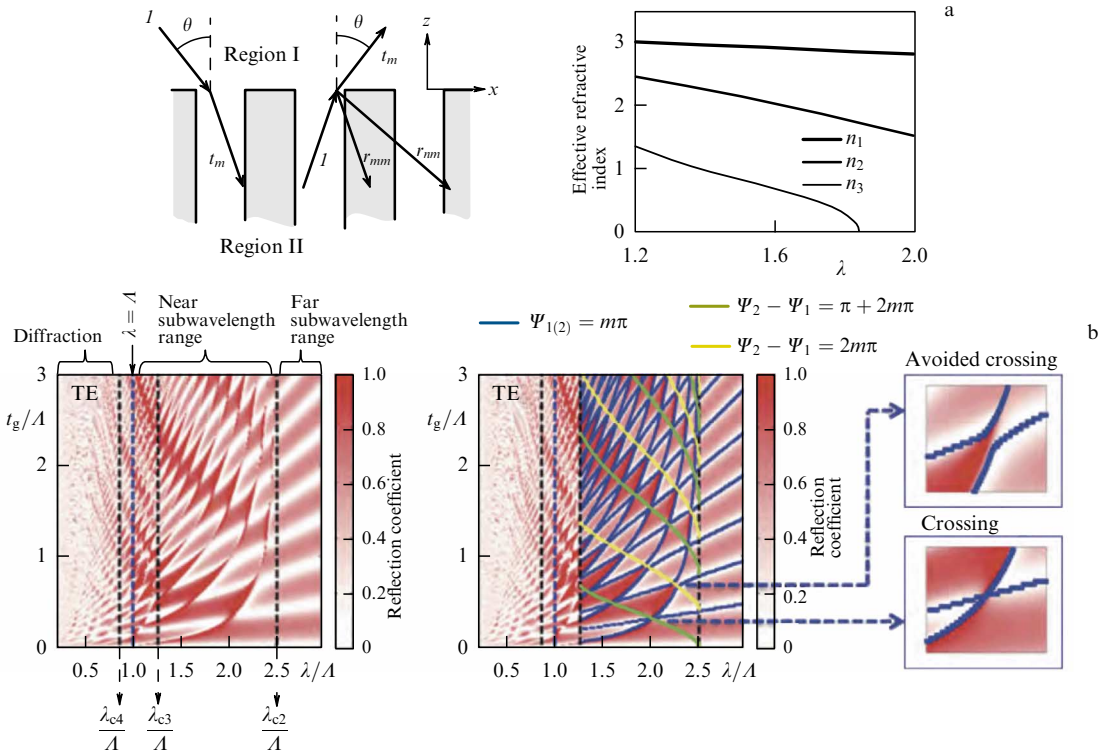

Figure 13. (a) Interface between a homogeneous medium and a semi-infinite 1D photonic crystal (left) and spectral dependence of effective propagation constants of Bloch modes in 1D photonic crystal (right). t_m is the coupling coefficient, r_{mn} is the reflection coefficient, indices $m, n = 1, 2, 3, \ldots$ are the numbers of the corresponding Bloch mode. (Adapted from [159].) (b) Reflection coefficient maps for 1D photonic crystal slab: cut-off wavelengths of the Bloch modes divide the map into areas with single-mode, two-mode, and multiple-mode regimes (left). In the right part of the figure, blue lines identify the single-mode Fabry–Perot resonances, green and yellow lines indicate conditions under which first and second modes are combined upon in-phase and anti-phase re-reflection. (Adapted from [160].)

Above, we considered gratings with up-down mirror symmetry. However, BICs can exist in gratings without such a symmetry. This problem was considered by Ndangali and Shabanov [69] and Bulgakov et al. [44]. In the latter paper, the authors considered a grating consisting of a slab with ridges periodically arranged either on top or on both sides of the slab (Fig. 14a). In the case of two gratings, it was assumed that they have the same period, but different permittivities, and can be shifted with respect to each other by distance a. The authors of [44] demonstrated that, if a two-sided grating possesses either mirror symmetry with respect to the xy plane or glide symmetry, i.e., a composition of mirror reflection in the xy plane and a half-period translation along the x-axis, then the BICs are stable against variation of parameters as long as these symmetries are preserved. In this case, only a shift of the BIC along the dispersion curve occurs. If the up-down symmetry is broken due to the different geometries or material parameters of the lattices, the existence of the accidental off-Γ BIC requires a fine adjustment of the system parameters. Therefore, such BICs are not robust against variation of the material or geometrical parameters of the structure. The obtained results are in complete accordance with those obtained earlier by Ndangali and Shabanov [69], who considered double arrays of thin dielectric rods shifted with respect to each other as shown in Fig. 14b. The authors of [69] established that an arbitrary shift of one grating with respect to the other one results in the symmetry-protected BIC turning into an accidental BIC, and the accidental BIC turning into a high-Q quasi-BIC. In addition, they showed that BICs can exist if two or three diffraction channels are open, but the formation of these BICs requires an adjustment of the radius and permittivity of the rods.

Ndangali and Shabanov [69] considered BICs in an array of very thin rods, the Rayleigh approximation being applicable to each of them, i.e., $\sqrt{\varepsilon}\,k_0 R \ll 1$, where k_0 is the wavenumber in a vacuum, R is the radius of the rods, and ε is their permittivity. Bulgakov and Sadreev [70] generalized the considered problem to the case of arbitrary radius R and permittivity ε using the multiple scattering theory in the T-matrix formalism [173–175]. They considered an array of GaAs rods with $\varepsilon = 12$ and the size parameter $\sqrt{\varepsilon}\,k_0 R$ in the range from 1 to 10. They showed that such a system supports three types of BICs: (i) symmetry-protected BICs with a zero Bloch vector, (ii) BICs embedded in one open diffraction channel with a nonzero Bloch vector, (iii) BICs embedded in two and three open diffraction channels. The first and second BIC types exist for a wide range of material parameters of the rods, whereas the third one occurs only at specifically chosen values of the rod radius or permittivity. Yuan and Lu [176] considered a similar system numerically and determined the domains of BIC existence in the parametric space (R, ε). Bulgakov and Maksimov [121] studied finite arrays consisting of N parallel dielectric rods and analyzed the dependence of quasi-BICs and resonances below the light cone (guided-mode resonance) on N. They identified two types of BICs with radiative Q factors scaled as $Q_{\mathrm{rad}} \sim N^2$ and $Q_{\mathrm{rad}} \sim N^3$.

As we discussed in Section 3.4, BICs in periodic structures can be considered polarization vortices with a certain topological charge. With a variation in the system parameters, these vortices manifest nontrivial dynamics in **k**-space, including annihilation, merging, and decay. All these effects were

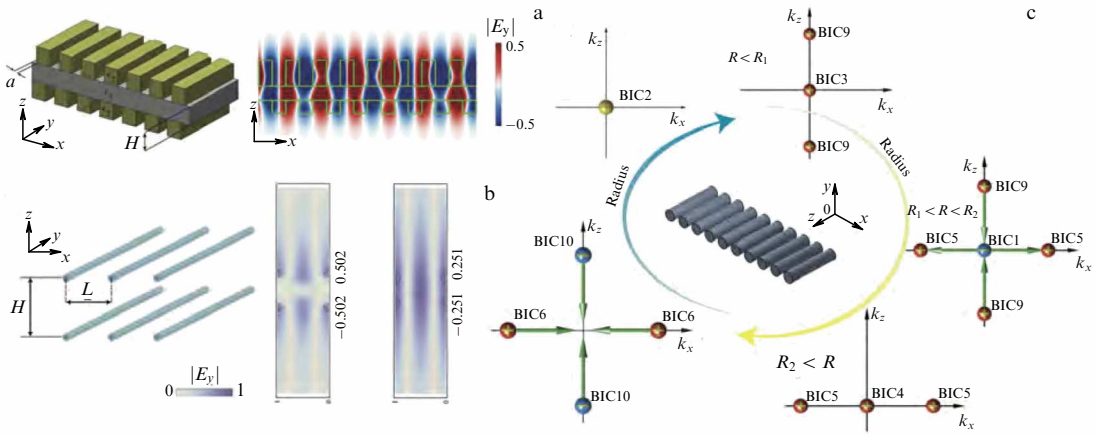

Figure 14. BICs in one-dimensional periodic structures. (a) Schematic of a double grating and E_y-field pattern of an accidental off-Γ BIC. Parameter a is the shift in the xy plane, and H is the distance between layers. (Adapted from [44].) (b) Schematic view of a periodic structure composed of two arrays of dielectric rods and the E_y-field pattern of accidental in-Γ BICs. (Adapted from [69].) (c) Topological charge dynamics in a grating composed of dielectric rods. Yellow and blue arrows indicate two different eigenmodes. (Adapted from [177].)

clearly demonstrated numerically in Ref. [177] by the example of BICs in a periodic array of parallel dielectric rods. Figure 14c shows the evolution of topological charges for two families of BICs belonging to different dispersion branches (photonic bands). Following the direction of the yellow arrow indicating an increase in the radius of the rod, one can see that the symmetry-protected BIC (BIC 3) with $q = 1$ decays into two accidental BICs with $q = 1$ (BIC 5) and one symmetry-protected BIC with $q = -1$ (BIC 1). A further increase in the radius results in the merging of two accidental BICs (BIC 9) at the Γ point with the symmetry-protected BIC (BIC 1). It is worth mentioning that, due to $\omega(-\mathbf{k}) = \omega(\mathbf{k})$ symmetry, off-Γ BICs emerge and disappear in pairs. The annihilation of topological charges at the Γ point may lead to the creation of both accidental and symmetry-protected BICs. The type of the forming BIC is determined by the total topological charge conservation law. Figure 14c (evolution along the blue arrow) illustrates the creation of the accidental in-Γ BIC with $q = 0$, when two BICs labelled BIC 6 with $q = 1$ merge with two BICs labelled BIC 10 with $q = -1$.

The value of topological charge determines the asymptotic dependence of the radiative Q factor on the Bloch wavenumber. Due to C_2 symmetry, one-dimensional periodic structures can support BICs with $q = 0$ or $q = \pm 1$ [43]. The Q factor of an isolated BIC with $|q| = 1$ scales as $Q \sim 1/(k \pm k_{\mathrm{BIC}})^2$ [45, 177, 178]. For example, the Q factor of the symmetry-protected BIC decreases as k^{-2}. Upon approaching the point of the annihilation, the dependence changes to $Q \sim 1/(k - k_{\mathrm{BIC}})^2(k + k_{\mathrm{BIC}})^2$ for both accidental in-Γ BICs and symmetry-protected BICs. The inverse fourth-power dependence indicates that the Q factor can be very large, even when $|k - k_{\mathrm{BIC}}|$ is not small [178]. However, if the system parameters are greatly detuned from this regime, the Q factor of the symmetry-protected BICs decreases as $Q \sim 1/k^2$ again. These asymptotic dependences are extremely important, as they determine the radiative losses of quasi-BICs in finite-size structures and their robustness to disorder [45, 64, 125].

4.2 1D periodicity with axial symmetry

One-dimensional periodic structures with axial symmetry (corrugated cylindrical waveguides and chains of spheres or disks (see the inset in Fig. 15a below)) can also support different types of BICs. The theory of BICs in such structures was formulated by Bulgakov and Sadreev [124] and further developed in Refs [66, 92, 95]. Owing to the axial symmetry and periodicity of the structure along the z-axis, the solution can be written in the following form:

$$\mathbf{E}(r, \varphi, z, t) = \mathbf{u}_{m,k_z}(r, z)\, \exp(-\mathrm{i}\omega t \pm \mathrm{i}k_z z \pm \mathrm{i}m\varphi), \quad (20)$$

where φ is the azimuthal angle, m is the azimuthal quantum number, k_z is the Bloch wavenumber, and $\mathbf{u}_{m,k_z}$ is a periodic function of z. In the case of $m = 0$, the solutions of Maxwell's equations in cylindrical coordinates can always be divided into TE and TM polarizations [179]. It is worth noting that, in contrast to uncorrugated waveguides, in the considered problem the solutions with $k_z = 0$ do not split into two independent polarizations, since k_z is a quasi-wavenumber, which is defined up to the reciprocal lattice vector. Thus, for $k_z = 0$ and $m \neq 0$, all the modes have hybrid TE–TM polarization, as do the modes with $m = 0$ and $k_z \neq 0$. Therefore, in subwavelength chains, the modes with $k_z = 0$ and $m = 0$ have only one open diffraction channel. For the modes odd with respect to reflection in the xy plane (Fig. 15a), the coupling to this diffraction channel vanishes because of symmetry, as happens in dielectric gratings. Therefore, subwavelength structures with a symmetric potential, $\varepsilon(-z) = \varepsilon(z)$, support the symmetry-protected BICs at the Γ point. For the modes with $m \neq 0$ at the Γ point, the radiative losses to one channel (TE or TM) can vanish due to the symmetry of the mode itself. The losses to the second channel can be suppressed by fine tuning the system parameters. Bulgakov and Sadreev in Ref. [180] referred to such states as partially symmetry-protected BICs and demonstrated that BICs with $m \neq 0$ and $k_z \neq 0$ can be produced by fine tuning the chain parameters. As we mentioned above, BICs in periodic chains can be characterized by a topological charge, similar to BICs in 2D periodic structures [92]. However, it is still unclear how to measure this charge.

BICs in periodic chains were first observed experimentally in the GHz frequency range, in a one-dimensional array of coupled ceramic disks (Fig. 15a) [64]. To observe a symmetry-protected BIC, two identical loop antennas playing the role of magnetic dipoles were used; they were placed coaxially with a chain and connected to ports of a vector network analyzer. The measured and calculated transmission spectra are shown

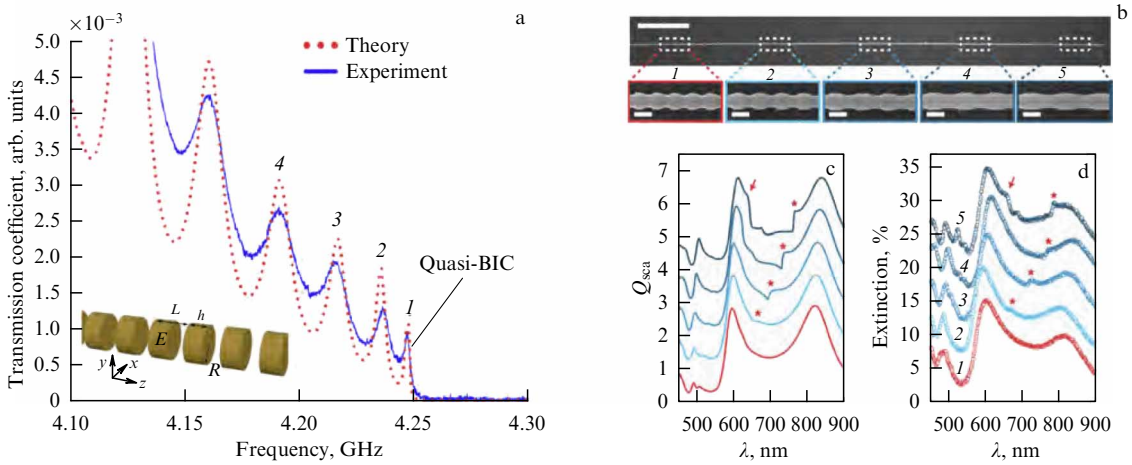

Figure 15. (a) Experimental transmission spectra of a chain consisting of 20 ceramic disks placed between two coaxially positioned loop antennas shown in the inset. Dotted line shows results of numerical simulations carried out in COMSOL MULTIPHYSICS. Rightmost peak corresponds to a quasi-BIC. (Adapted from [64].) (b) SEM image of a nanowire containing five sections of a superlattice; scale bar is 10 μm. Calculated scattering efficiency spectra (c) and experimental extinction spectra (d) (spectra offset by 5%) for geometric superlattices. (Adapted from [181].)

in Fig. 15a. The last peak in the spectrum corresponds to a quasi-BIC, which transforms into a genuine BIC in an infinite chain. It was shown that the total Q factor of the quasi-BIC Q_{tot} first grows quadratically with the increase in the number of periods and then saturates at the level of $Q = 4000$ due to material absorption. An accidental BIC ($m = 0$, $k_{\text{B}} = 0$) was also observed experimentally in a similar system in Ref. [125]. The linear growth of the Q factor with the number of disks was demonstrated for an observed accidental off-Γ BIC. Such a behavior of the Q factor in this state substantially differs from that of an accidental BIC in the center of the Brillouin zone, for which the radiative Q factor grows as $Q \sim N^3$ with an increase in the number of scatterers in the array [121].

The first experimental observation of a BIC in structures with axial symmetry in the optical range was reported in 2019 [181]. The authors of Ref. [181] fabricated a silicon nanowire with a periodic grating on the surface (Fig. 15b). The surface grating forms a structure similar to a periodic array of disks placed coaxially on a common core. The nanowire was illuminated by a normally incident plane wave; as a result, quasi-BICs with different m were excited. The authors analyzed both theoretically and experimentally how the appearance of a BIC depends on illumination and the geometry of the cylindrical nanowire. Light confinement in such structures can be used to significantly enhance the absorption, which finds applications in photodetector or photovoltaic devices based on the p–i–n diode design and implemented in nanowires with superlattices [182].

Nanowires with periodic superlattices and arrays of disks have a number of advantages over an array of spheres due to a larger number of degrees of freedom. So, by independent adjustment of the period, height, and radius of the disks, one can provide high-precision engineering of mode composition, and obtain several BICs with different angular numbers and Bloch vectors. Such linear chains supporting BICs can be used as a compact source of optical beams with given angular momentum.

4.3 2D periodicity and photonic crystal structures

In this section, we consider the main properties of BICs in photonic crystal slabs (waveguides) — 2D periodical dielectric photonic structures that have a band gap for waves propagating in the waveguide plane. Confining light in the direction orthogonal to the structure plane is implemented at the expense of the refractive index difference. Since the 1990s, such structures have been considered simpler to fabricate than photonic crystals with full three-dimensional band gaps; in addition, they possess many useful properties of gratings [183, 184]. Compared to 1D structures, photonic crystal waveguides offer a broader variety of designs for unit cells with different types of arrangements and, consequently, more degrees of freedom for flexible control of their optical properties [156, 185]. Due to this fact, in the 2D case, BICs are much more diverse than in the case of 1D gratings or chains. In particular, in photonic-crystal waveguides, it is possible to obtain BICs with high ($\geqslant 2$) topological charges [43] and to form BICs robust to structural disorder [45].

The first systematic study of BICs in photonic crystal waveguides was carried out in 2013 [46] for a Si_3N_4 waveguide with a periodic array of circular holes (Fig. 16a). The waveguide was grown on an SiO_2/Si substrate and immersed in a liquid index-matched to silica to keep the up-down reflection symmetry required to observe accidental BICs. The band structure for TM-type modes along the Γ–X direction is shown in Fig. 16b. From Fig. 16c, it is seen that the structure supports a symmetry-protected BIC at the Γ point and an accidental BIC on a nonzero Bloch vector corresponding to an incidence angle of about 35°. The oblique red crosses show the values of the radiative Q factor calculated from the total Q factor, which was extracted from the measured reflection spectrum assuming the value of the nonradiative Q factor equal to 10^4. The achieved value of the radiative Q factor for the accidental BIC is of the order of 10^6; however, because of parasitic and nonradiative losses, the value of the total Q factor remains limited to 10^4. As far as we know, the results of Ref. [48] were the first direct experimental evidence of the existence of true accidental BICs.

The physics and origins of accidental BICs were analytically described in Ref. [186] within the framework of the coupled-wave theory (CWT), adapted to describe the response of 2D photonic crystal waveguides [187]. According to the analytical model, the electromagnetic fields of eigenmodes of a photonic system can be expanded in guided

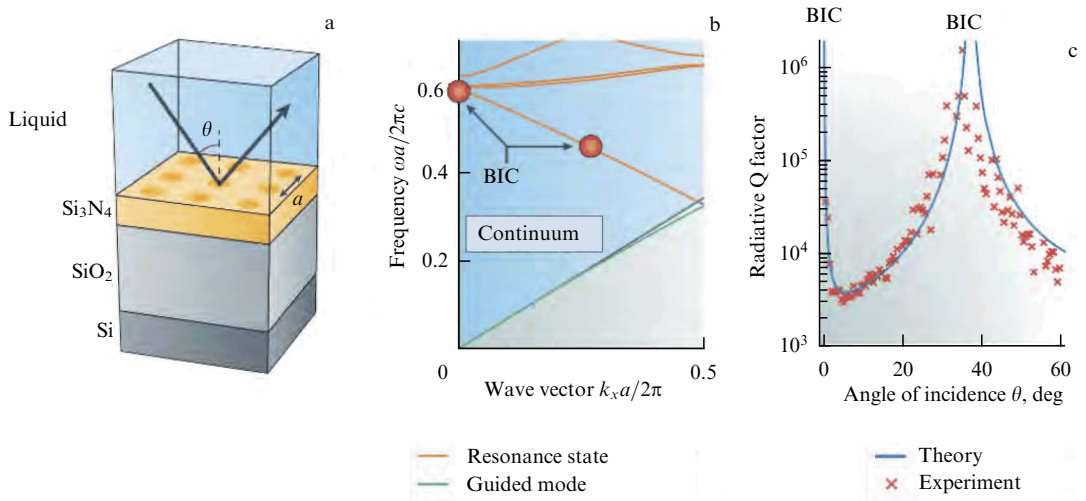

Figure 16. (a) Schematic layout of the experimental structure, immersed in a liquid, index-matched to silicon oxide at a wavelength of 740 nm. (b) Band diagram for TM polarization along the Γ–X direction. BICs are marked by red dots. (c) Normalized radiative lifetime extracted from the experimentally measured reflectivity spectrum (X's). Curve shows the result of modeling by the finite-difference method. (Adapted from [46].)

modes and leaky modes of a uniform waveguide, which are used as basis functions. Due to the interaction with the lattice, the guided modes also have radiative losses. Thus, both the guided and leaky modes can contribute to the same radiation channels (channels of diffraction) due to the interaction with the periodic potential of the structure. In Ref. [186], it was shown that accidental BICs appear due to the destructive interference of all the basis functions, both guided and leaky ones. Two reasons for destructive interference were indicated. First, the contributions from equivalent directions in the reciprocal space can result in the spontaneous appearance of an additional symmetry and, therefore, to the formation of an accidental BIC. An example of such a BIC is presented in Ref. [46]. Second, it was shown that accidental BICs do not necessarily occur exactly at a high-symmetry point in the reciprocal space. The reason is that, for accidental BICs, the guided basis modes contribute to the open radiation channels of the photonic structure with different weights and, therefore, after blocking the radiation at the symmetry point, some residual radiation can still remain. In other words, the point corresponding to a BIC in the reciprocal space does not always have a high symmetry, but is close to it. This is typical of the Friedrich–Wintgen mechanism [7, 188]. Moreover, it was shown analytically that the positions of accidental BICs can be shifted by changing various parameters, such as the waveguide cladding permittivity or geometrical sizes. It is worth mentioning that, in other papers, analytical considerations demonstrate that the energy of symmetry-protected BICs is mainly concentrated in the closed diffraction channels of the ± 1 orders.

The relatively moderate value of the total Q factor of 10^4, obtained in Ref. [46], is related to the losses at the sample edges arising due to the finite size of samples and fabrication imperfections. Recently, a new approach was suggested, which allows a suppression of such losses using the topological nature of BICs, namely, by merging several BICs at the Γ point in the k-space [45, 189]. Reference [45] considered a 2D dielectric photonic crystal membrane suspended in air. The fundamental TE band of the membrane supported one symmetry-protected BIC at the Γ point and eight accidental BICs located symmetrically around the Γ point. The tunability of accidental BICs allows moving them away from an off-Γ position to the center of the Brillouin zone. The experimentally measured value of 5×10^5 was demonstrated for the total Q factor in the merging regime. For a single isolated BIC with a charge of ± 1, the Q factor of a standard symmetry-protected BIC decays quadratically, $Q \sim 1/k^2$, with distance from the Γ point. When all nine BICs merge, it turns out that $Q \sim 1/k^6$. Later, it was shown that, for finite-size samples, the highest Q factor can be achieved not under the condition of complete merging but in the pre-merging regime, when the accidental BICs lie on a small-radius circle in the k-space [116].

One of the distinctive features of 2D periodic photonic structures is that a BIC can exist even in chiral samples without the in-plane inversion symmetry [190]. In general, a BIC in the sub-diffractive regime can be achieved by zeroing the amplitudes of radiation into both polarization channels. The authors of Ref. [190] showed that, by using a periodic photonic structure with cross-shaped elements and possessing no second-order symmetry axis, it is possible to zero the radiation amplitudes for both polarizations: one polarization channel is suppressed due to the vertical mirror plane, and the other one, parametrically, by tuning the unit cell geometry. This mechanism of BIC formation is very similar to the one considered by Bulgakov and Sadreev for obtaining partially symmetry-protected BICs in a chain of dielectric spheres [180]. It was later shown that such an approach allows combining the strong linear and nonlinear circular dichroism, accompanied by a significant field enhancement caused by the BIC [191].

4.4 Individual subwavelength resonators

For individual subwavelength resonators, genuine nonradiative states require extreme values of permittivity, tending toward infinity or zero at the resonance frequency [60, 194, 195] or imitating periodic boundary conditions by means of metallic waveguides [62, 196, 197]. In realistic individual resonators, there is always an infinite number of radiation channels, which limits the Q factor substantially. However, the concept of quasi-BICs allows approaching virtually nonradiative states in individual dielectric resonators. Using the parameter-tuning approach originally developed by

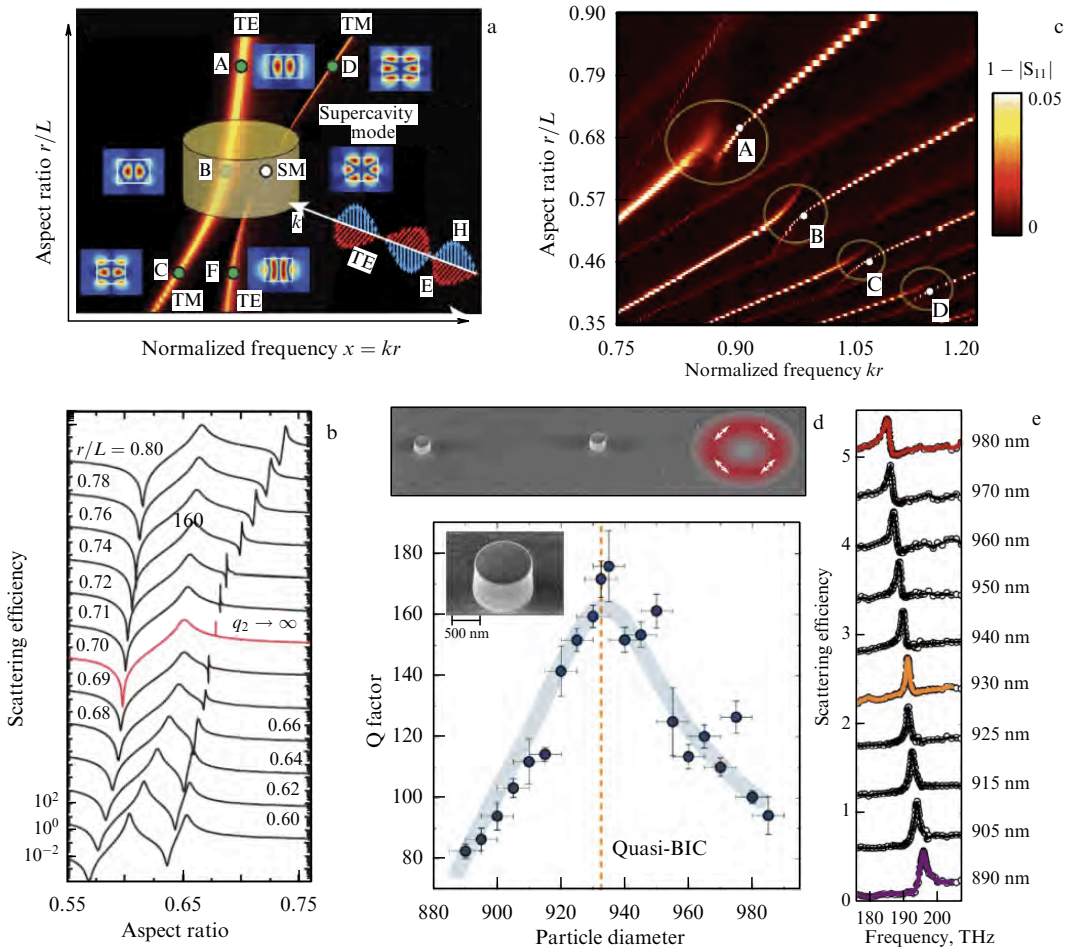

Figure 17. (a) Illustration of strong mode coupling and formation of a bound state in the continuum in a high-index dielectric resonator. (b) Simulated scattering spectra of a nanodisk with $\varepsilon = 80$ and azimuthal index $m = 0$. Red color marks the spectrum corresponding to a quasi-BIC. (Adapted from [188].) (c) Results of measuring the reflection coefficient $1 - |S_{11}|$ for a ceramic nanodisk with $\varepsilon = 44.8$ versus frequency kr and aspect ratio r/L. Quasi-BICs labeled A–D correspond to aspect ratios $r/L = 0.71$, 0.55, 0.47, and 0.42, respectively. (Adapted from [192].) (d) Scanning electron microscopy (SEM) image of nanodiscs and electric field distribution for an azimuthally polarized incident wave (upper part of the figure) and the quasi-BIC Q factor extracted from experimental spectra depending on the disk diameter. (e) Experimental reflectance spectra of nanodisks with different diameters. (Adapted from [193].)

Friedrich and Wintgen [7] and later used for some other geometries [198], one can create high-Q quasi-BICs in geometrically compact resonators at subwavelength scales. In recent paper [199], it was proposed to implement quasi-BICs, referred to there as supercavity modes, in individual dielectric resonators by continuously changing the geometric shape of the resonator. Such parameter tuning enables destructive interference and strong coupling of two leaky modes (radial and axial) when their frequencies come close. It is of importance that the modes forming a quasi-BIC possess the same symmetry.

The mentioned concept of a supercavity mode is illustrated in Fig. 17a. Figure 17b demonstrates the contribution of modes with a zero azimuthal index to the scattering cross section of a high-index dielectric cylinder depending on the dimensionless frequency and aspect ratio. The radial and axial modes interact strongly in the vicinity of the avoided crossing point, which results in a sharp narrowing of the linewidth for one of the modes — the supercavity mode. The second mode linewidth increases according to the general properties of open non-Hermitian systems [55] (Fig. 6b). The hybrid mode profiles shown in Fig. 17a are a combination of radial and axial oscillations in the vertical cross section and a uniform azimuthally symmetric distribution in the horizontal cross section. The formation of quasi-BICs can be detected by the special features of the lineshape in the scattering spectrum. For a cylinder with high permittivity ($\varepsilon = 80$), the lineshape changes from an asymmetric Fano profile to a symmetric Lorentzian in the vicinity of supercavity mode formation, as shown in Fig. 17b. The transformation of the Fano profile into a Lorentzian corresponds to the diverging Fano asymmetry parameter q. Such a behavior was later explained by the interference of different modes with close far-field profiles [200, 201]. In the considered case (Fig. 17b), both interacting modes are dominated by magnetic dipolar contribution. Upon interference of the mode, the dipole contributions can cancel each other, thus making dominant the next allowed multipole (in this case, magnetic octupole) contribution . The formation of quasi-BICs with nonzero azimuthal indices is also possible, but it leads to lower Q factors because of the lower symmetry of the field profile.

The first experimental observation of quasi-BICs was carried out quite recently in the microwave [192] and near-IR [193, 202] ranges. Figure 17c shows the experimental map of the reflection coefficient $1-|S_{11}|$ for a single ceramic disk

with a permittivity of 44.8 [192]. The excitation was performed in the near field with a loop antenna, which selectively excites the modes with a zero azimuthal index. Four avoided resonance crossings corresponding to the formation of quasi-BICs are marked in the spectra. The radiative Q factor of quasi-BICs reaches 200,000. However, due to the absorption in the ceramic material, the maximal measured unloaded total Q factor is restricted to a value of 12,500. The observation of supercavity modes in the near-IR range was carried out for isolated AlGaAs nanodisks on a three-layer substrate with a reflective layer of indium-tin oxide (ITO) in the middle [193, 202]. The SEM image of individual nanodisks is shown in the inset to Fig. 17d. The measured spectra and extracted Q factor for a range of disk diameters are shown in the lower part of Fig. 17d. The maximum measured Q factor is about 180 for a disk 930 nm in diameter. The spectra show (Fig. 17e) that the line has a Fano resonance shape and changes its asymmetry in the vicinity of the quasi-BIC, as was predicted theoretically for a single disk in a vacuum. To match the mode and excitation symmetry, a tightly focused azimuthally polarized Gaussian beam was used.

Later, several generalizations were suggested for quasi-BICs in nonperiodic finite-size resonators. For example, two coaxial disks were shown to support quasi-BICs with much higher Q-factor values than those of each disk separately [203]. Additionally, it was proposed to use Bragg reflectors to increase further the Q factor of a single disk [204]. Subsequently, the multipolar classification of eigenmodes in single resonators of different shapes was suggested, based on the symmetry group theory [205]. These results lead to a prediction of quasi-BICs in dielectric spheroids [206], triangular [205] and rectangular prisms [207], and resonators of arbitrary shapes [208].

4.5 Asymmetric metasurfaces and quasi-bound states in the continuum

As was recently demonstrated, the transmission spectra of dielectric metasurfaces with broken unit cell symmetry, recorded under normal incidence, demonstrate very narrow peaks, which are associated with quasi-BIC excitation [106]. It was established that in-plane asymmetry induces an imbalance of the interference between counterpropagating leaky waves, resulting in the formation of a quasi-BIC. Hence, it is possible to control the radiative losses in quasi-BICs with high accuracy. This effect was experimentally observed in a variety of metasurfaces in various frequency ranges and was discussed in connection with electromagnetic field-induced transparency [209], tunable high-Q resonances [210], trapped-mode resonances [211], broken-symmetry Fano metasurfaces [212, 213], and dark modes [214].

Figure 18a illustrates the scattering of light by an asymmetric metasurface. The radiative Q factor of quasi-BICs in asymmetric metasurfaces is described by the typical inverse quadratic dependence on the meta-atom asymmetry parameter α [106], as shown in the left panel of Fig. 18b. In the regime of transmission (or reflection), quasi-BICs manifest themselves as sharp asymmetric Fano resonances, whose width and depth decreases with the decrease in α, as shown in the right part of Fig. 18b. The total Q factor of the quasi-BIC mode is limited by other losses (see Section 3.5). Due to the parasitic effect of other losses, the maximum field enhancement can be achieved not for minimum radiative losses but in the regime of optimal (critical) coupling, when the rates of radiative and parasitic losses are equal, $Q_{abs} = Q_{rad}$ [110, 111]. Recently, quasi-BICs with huge values of the Q factor have been experimentally demonstrated in silicon metasurfaces with different designs of meta-atoms. Figures 18c, d show SEM images of two metasurfaces hosting quasi-BICs with Q factors of about 18,500 [115] and 750, [215], achieved by smart engineering of radiative losses using advanced electron-beam tomography techniques. Later, it was shown that even a true BIC can exist in an asymmetric metasurface under specific conditions [190]. In addition, metasurfaces with strong asymmetry were used to create a strong chiral response [216–218].

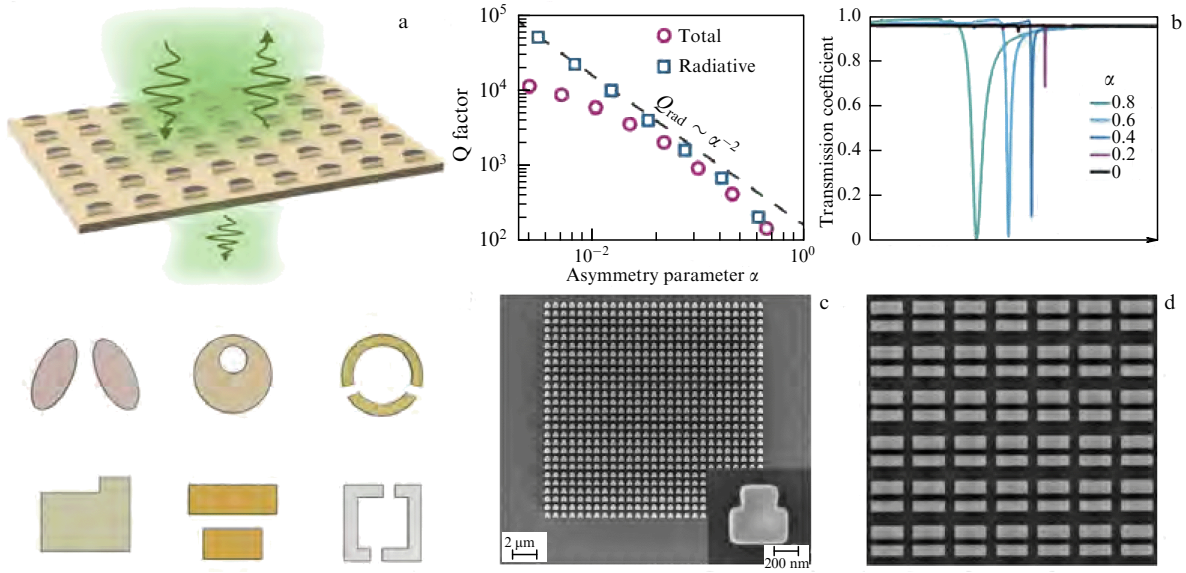

Figure 18. (a) Schematic of the scattering of light by a metasurface and examples of unit cells of asymmetric metasurfaces with a broken in-plane inversion symmetry of constituent meta-atoms supporting sharp resonances. (b) Typical dependence of total (circles) and radiative (squares) Q factors of a BIC on the meta-atom asymmetry parameter α, as well as the change in the transmission spectrum upon variation of α. (c, d) SEM images of a silicon metasurface created for the recent experimental demonstration of quasi-BICs with very high Q factors of approximately 18,500 (c) and 750 (d). (Adapted from [106, 202].)

5. Applications of bound states in the continuum

BICs and quasi-BICs are widely used for various applications in photonic crystal slabs, waveguides, single subwavelength particles, and other platforms. BIC-based applications include filtering [221–224], lasing [68, 88, 96, 116, 225–231], magnetophotonics [232, 233], detection of biological objects [215, 219, 220, 234–242], nonlinear generation and self-action [22, 26, 111, 117, 118, 178, 243–254], vortex generation [90, 98, 225], on-chip photonic devices [93, 224, 256–258], switches driven by external voltage [259], active THz devices [260], optical tuning of halcogenide metasurfaces [261], enhancement of chiral nonlinear response [191], and harmonic generation in hybrid structures with monolayers of transition metal dichalcogenides [262, 263]. Moreover, BICs in single nanoparticles were used to achieve a record-high efficiency of second-harmonic and higher harmonic generation [202, 264–266], the generation of quantum-entangled photons [267], and low-threshold lasing [84].

Let us consider some applications in more detail. Passive photonic structures supporting BICs have recently been used to increase the efficiency of detecting biological objects. Tittl et al. [219] implemented a nanophotonic sensor of biomolecules in the mid-IR range, based on the reflection from a dielectric matrix of metasurfaces supporting BICs. Figure 19a shows SEM images of an asymmetric silicon metasurface and its meta-atoms. The proposed structure supports quasi-BICs in the mid-IR range with a Q factor of approximately 200. Figure 19b presents reflection images of a pixel metasurface obtained for four given wavelengths and normalized reflection spectra for 21 out of 100 metapixels. Due to the narrow quasi-BIC resonance in the reflection spectrum and its tunability with changes in the geometric dimensions of the metasurface, a method based on this structure for distinguishing the absorption spectra of various molecules was demonstrated. Leitis et al. [220] used an asymmetric silicon metasurface with BICs for angle multiplexing of spectra, which also allowed a convenient distinguishing of absorption spectra of various biomolecules. Figure 19c shows a metasurface multiplexing scheme and Fig. 19d presents the spectra of reflection from the structure. In a series of papers by Romano et al. [127, 238, 268], the sensitivity of sensors based on photonic crystal waveguides with BICs to changes in the refractive index of the external medium was studied, and it was experimentally shown that, due to the BICs, a high sensitivity can be achieved. In a recent paper by Jahani et al. [242], silicon metasurfaces with a complex unit cell were developed using BICs to detect extracellular vesicles of cancer cells.

Photonic structures with BICs are widely used in active photonics, in particular, to generate laser radiation. Figure 20a shows output power spectra depending on the wavelength and pump power for a 16×16 metasurface supporting BICs in the near-IR range from [68]. In this paper, the authors used a tunable accidental BIC with a wavelength of 1550 nm. The right part of Fig. 20a shows the dependence of the output power on the pump power at resonance. As the pump power is increased to 60 μW, a distinct peak is observed in the emitted power spectra at the BIC wavelength. The inset shows a SEM image of the structure. In recent paper [116], lasing from a so-called super-BIC, i.e., several BICs coincident in the phase space and having the same frequency, was studied. A distinctive

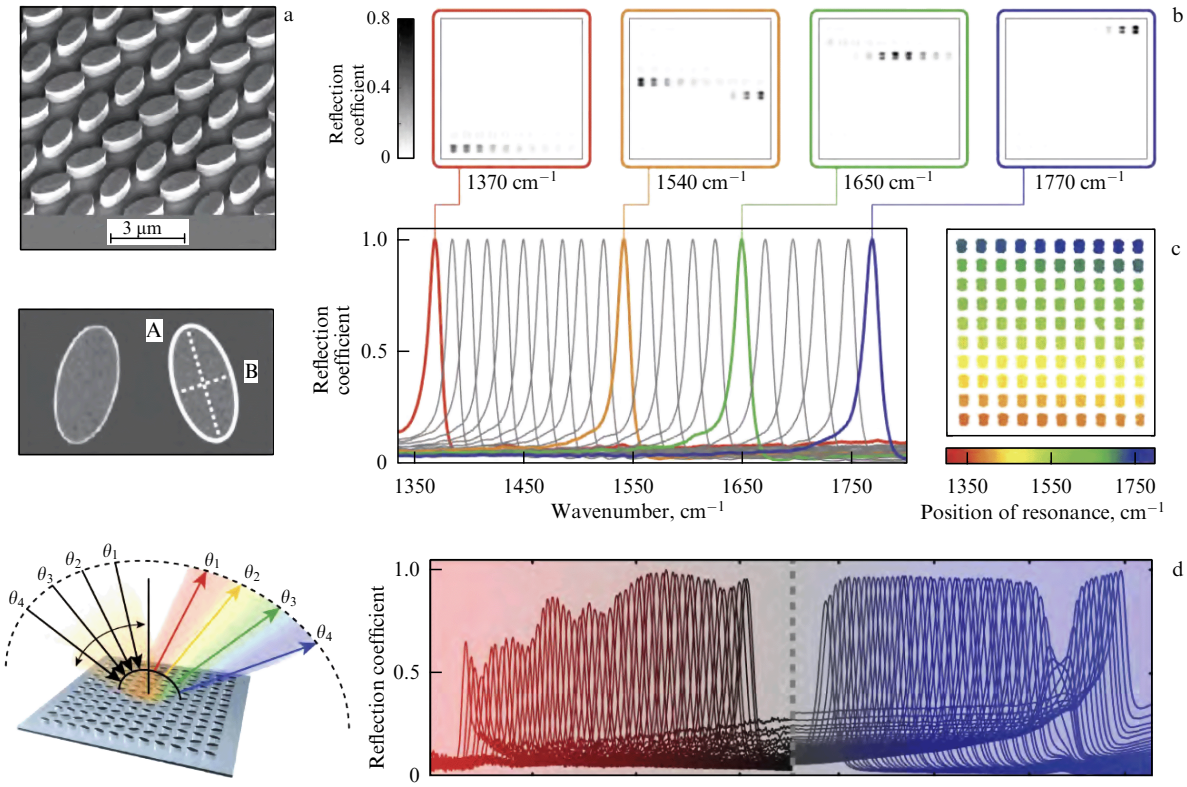

Figure 19. (a) SEM image of a metasurface and its meta-atom. (b) Reflection images of a pixel metasurface obtained for four given wavelengths in the mid-IR range. Normalized reflection spectra for 21 out of 100 metapixels. (Adapted from [219].) (c) Germanium-based dielectric metasurface supporting a quasi-BIC with angle multiplexing. (d) Reflection spectra after deposition of a thin film of polymethyl methacrylate with centrifugation. (Adapted from [220].)

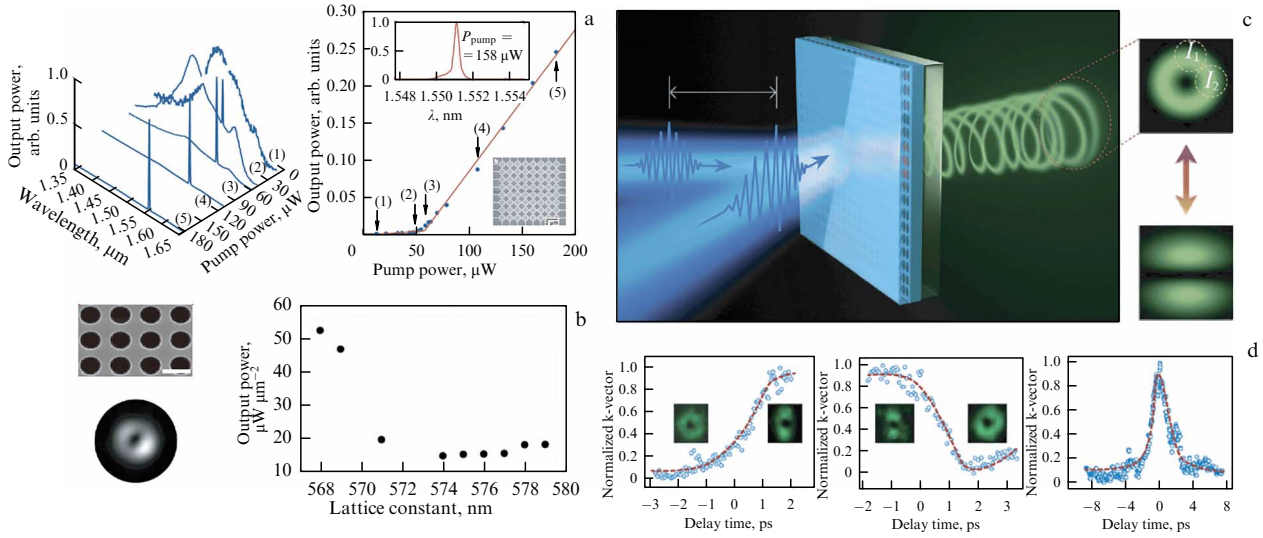

Figure 20 (a) Change in the normalized output power depending on the wavelength and pump power for a metasurface. Output power as a function of the average pump power (light curve) at the lasing wavelength. Image of a 16 × 16 metasurface is shown in the inset. (Adapted from [68].) (b) SEM image of a photonic crystal waveguide and measured far-field profile for a super-BIC laser. Value of the lasing threshold normalized to the pumping area (5.4 μm in size) as a function of the lattice parameter. (Adapted from [116].) (c) Schematic of a two-beam pumping experiment. Insets show far-field radiation patterns of a perovskite photonic structure for symmetric and asymmetric pump beam profiles. (d) Transition from vortex lasing to linearly polarized lasing and the reverse process. Transition from an annular beam to a two-lobe beam and back on the scale of several picoseconds. (Adapted from [96].)

feature of a super-BIC is the higher mode resistance against deviations from periodicity and imperfections in the structure surface. Figure 20b shows a SEM image of an InGaAsP photonic crystal waveguide and the measured far-field profile for a mode of the super-BIC laser. Laser oscillation in the structure is achieved through the use of quantum dots in the layer. As shown in Fig. 20b, the spot in the Fourier space has a small angular divergence, which is a hallmark of strongly localized modes. The right part of Fig. 20b shows the lasing threshold normalized to the pumping area (5.4 μm in size) as a function of the lattice parameter of the structure. The super-BIC state is realized at a lattice parameter of about 573 nm; in this regime, the lasing threshold is minimum and has a record-low value among all BIC lasers and lasers based on topologically protected states [116]. Huang et al. [96] studied vortex microlasers based on perovskite photonic crystal waveguides supporting BICs in the visible range for ultrafast optical switching at room temperature. Switching between generating a vortex beam and a linearly polarized beam, with a characteristic switching time from 1 to 1.5 picoseconds and a record-low power consumption, is experimentally demonstrated. Figure 20c shows a schematic diagram of the experiment on two-beam pumping of a perovskite photonic structure. The insets show far-field radiation diagrams for symmetric and asymmetric pump beam profiles. Figure 20d shows the transition from vortex to linearly polarized lasing and the reverse process on the scale of several picoseconds.

S Ha et al. [227] studied a laser based on a gallium arsenide metasurface supporting a BIC at a wavelength of about 825 nm. Azzam et al. [229] studied single-mode and multimode lasing in the visible range based on a similar titanium dioxide metasurface coated with a thin layer of an organic dye. It was experimentally shown that, due to the BIC properties, directed radiation can be obtained by adjusting the period of the metasurface. In the recent paper by Yang et al. [231], lasing based on an asymmetric Si_3N_4 metasurface coated with a strongly fluorescent rhodamine 6G dye was studied. Lasing at a wavelength of approximately 600 nm due to the excitation of a quasi-BIC was experimentally demonstrated. S Dyakov et al. [88] showed a significant increase in photoluminescence from a silicon photonic-crystal waveguide with germanium nanoislets, which supports BICs in the near-IR range.

BICs and quasi-BICs are studied most actively in nonlinear optics and photonics applications, mainly in order to enhance nonlinear generation and to observe the self-action of an exciting pulse. In a series of papers by K Koshelev et al. [111, 269], optical second and third harmonic generation was studied in nonlinear dielectric metasurfaces with an asymmetric unit cell, supporting quasi-BICs with the Q factor depending on the asymmetry. In particular, in [111], the fabricated metasurface had a low Q factor of approximately 160 due to the presence of strong surface roughness. It was shown theoretically and experimentally that, for such nonperfect photonic structures, the highest efficiency of harmonic generation is achieved not at the highest Q factor but in the critical coupling regime, when the radiative Q factor is equal to the Q factor related to all the other types of losses. It was also shown that the critical coupling regime can be achieved by changing the asymmetry parameter of the meta-atom, which should be taken into account in the design of resonant nonlinear metasurfaces. G Zograf et al. [253] studied the generation of higher-order odd harmonics (3, 5, 7, 9, 11) from an asymmetric silicon metasurface, shown schematically in the left part of Fig. 21a. The right part of Fig. 21a shows the spectra of optical harmonics in the regime of excitation with 100-fs pulses and the dependence of the output power on the pump power for an optimized metasurface, using the critical coupling criterion.The dependence of the output power on pump power in the range of 0.03–0.3 TW cm^{-2} is determined by the same law, regardless of the harmonic number, which allows a conclusion that the

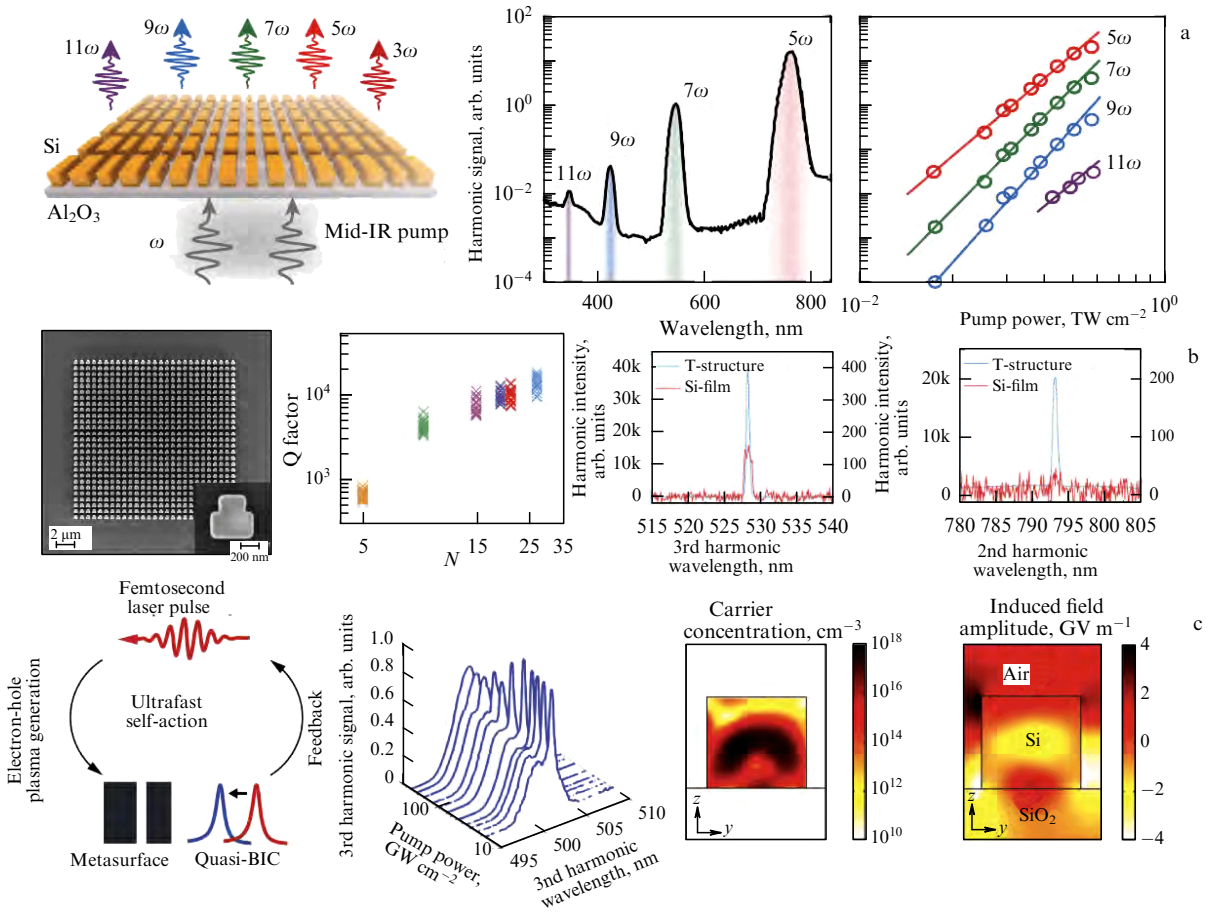

Figure 21. (a) Spectrum of the signal of the 3rd to 11th harmonic from an asymmetric silicon metasurface with BICs and dependence of the power of the harmonics on the pump pulse power. (Adapted from [253].) (b) Statistics of the measured Q factors of the BICs for all fabricated silicon metasurfaces with different sizes. Spectra of the second and third harmonics for a metasurface and an unstructured film. (Adapted from [115].) (c) Ultrafast self-action of a pulse through a BIC. Spectrum of the third harmonic depending on the pump power. Carrier concentration and induced field amplitude inside the nanostructure at a pump intensity of 240 GW cm^{-2}. (Adapted from [254].)

structure operates in a nonperturbative regime. The authors explain the transition to the nonperturbative regime through the mechanism of free-carrier generation in silicon due to multiphoton absorption. J Liu et al. [115] studied asymmetric silicon metasurfaces with T-shaped meta-atoms (Fig. 21b). A record-high Q factor of over 20,000 was achieved for a BIC in a structure with 26×26 periods due to the high quality of nanolithography and special features of the structure design. The measured spectra of the second and third optical harmonic signals are shown in the right panel of Fig. 21b; at the BIC wavelength, the harmonic signal increases by several times. I Sinev et al. [254] studied an asymmetric silicon metasurface for third harmonic generation at high pump intensities of the order of 0.3 TW cm^{-2}. It was demonstrated that, at a pump intensity higher than 240 GW cm^{-2}, self-action of a pulse occurs due to the generation of free charge carriers through the multiphoton absorption mechanism, schematically shown in the left part of Fig. 21c. The calculated induced field amplitude and charge carrier concentration at a peak intensity of 240 GW cm^{-2} reached 3 GW m^{-1} and 10^{18} cm^{-3}, respectively, as shown in the right part of Fig. 21c.

6. Conclusion

Bound states in the continuum have a long history in optics and radiophysics. However, today, research in this field is taking a new turn due to rapid progress in the physics of metasurfaces, 2D materials, nonlinear nanophotonics, flat optics, and related areas. BICs can be observed in a wide variety of photonic structures, including metasurfaces, photonic crystal slabs, high-contrast gratings, corrugated planar waveguides and fibers, ridge waveguides, linear chains, and many other systems. A relatively recent discovery is a new class of BICs in Bragg resonators with an anisotropic defect layer [270–273]. Today, the study of BICs is developing in acoustics [20, 274–276]. BICs are an illustrative example of how an idea suggested in one area of physics a century ago today affects many other areas and is already being used in a number of practical applications.

Acknowledgements. This study was carried out with financial support from the Russian Foundation for Basic Research (grant no. 20-12-50314).

References

1. von Neuman J, Wigner E *Phys. Z.* **30** 467 (1929)
2. Fonda L, Newton R G *Ann. Physics* **10** 490 (1960)
3. Stillinger F H, Herrick D R *Phys. Rev. A* **11** 446 (1975)
4. Stillinger F H, Weber T A *Phys. Rev. A* **10** 1122 (1974)
5. Robnik M *J. Phys. A* **19** 3845 (1986)
6. Pappademos J, Sukhatme U, Pagnamenta A *Phys. Rev. A* **48** 3525 (1993)
7. Friedrich H, Wintgen D *Phys. Rev. A* **31** 3964 (1985)

8. Nöckel J U *Phys. Rev. B* **46** 15348 (1992)
9. Cederbaum L S et al. *Phys. Rev. Lett.* **90** 013001 (2003)
10. Sadreev A F, Bulgakov E N, Rotter I *Phys. Rev. B* **73** 235342 (2006)
11. Herrick D R *Phys. B + C* **85** 44 (1976)
12. Stillinger F H *Phys. B + C* **85** 270 (1976)
13. Capasso F et al. *Nature* **358** 565 (1992)
14. Parker R *J. Sound Vibration* **5** 330 (1967)
15. Parker R *J. Sound Vibration* **4** 62 (1966)
16. Evans D, Levitin M, Vassiliev D *J. Fluid Mech.* **261** 21 (1994)
17. Ursell F *Proc. R. Soc. Lond. A* **435** 575 (1991)
18. Ursell F *Math. Proc. Cambr. Philos. Soc.* **47** 347 (1951)
19. Jones D S "The eigenvalues of $\nabla^2 u + \lambda u = 0$ when the boundary conditions are given on semi-infinite domains" *Math. Proc. Cambr. Philos. Soc.* **49** 668 (1953)
20. Lyapina A et al. *J. Fluid Mech.* **780** 370 (2015)
21. Marinica D, Borisov A, Shabanov S *Phys. Rev. Lett.* **100** 183902 (2008)
22. Bulgakov E N, Sadreev A F *Phys. Rev. B* **78** 075105 (2008)
23. Hsu C W et al. *Nat. Rev. Mater.* **1** 16048 (2016)
24. Sadreev A F *Rep. Prog. Phys.* **84** 055901 (2021)
25. Azzam S I, Kildishev A V *Adv. Opt. Mater.* **9** 2001469 (2021)
26. Koshelev K, Bogdanov A, Kivshar Yu *Sci. Bull.* **64** 836 (2019)
27. Koshelev K, Bogdanov A, Kivshar Yu *Opt. Photon. News* **31** (1) 38 (2020)
28. Plotnik Y et al. *Phys. Rev. Lett.* **107** 183901 (2011)
29. Kazarinov R F, Sokolova Z N, Suris R A *Sov. Phys. Tech. Phys.* **21** 130 (1976); *Zh. Tekh. Fiz.* **46** 229 (1976)
30. Vincent P, Nevière M *Appl. Phys.* **20** 345 (1979)
31. Paddon P, Young J F *Phys. Rev. B* **61** 2090 (2000)
32. Inoue M, Ohtaka K, Yanagawa S *Phys. Rev. B* **25** 689 (1982)
33. Sakoda K *Phys. Rev. B* **51** 4672 (1995)
34. Sakoda K *Phys. Rev. B* **52** 8992 (1995)
35. Cowan A R et al. *J. Opt. Soc. Am. A* **18** 1160 (2001)
36. Shipman S P, Venakides S *Phys. Rev. E* **71** 026611 (2005)
37. Bonnet E et al. *Opt. Quantum Electron.* **35** 1025 (2003)
38. Yablonskii A I et al. *Phys. Status Solidi A* **190** 413 (2002)
39. Henry C et al. *IEEE J. Quantum Electron.* **21** 151 (1985)
40. Avrutskii I A et al. *Sov. J. Quantum Electron.* **16** 1063 (1986); *Kvantovaya Elektron.* **13** 1629 (1986)
41. Robertson W M et al. *Phys. Rev. Lett.* **68** 2023 (1992)
42. Pacradouni V et al. *Phys. Rev. B* **62** 4204 (2000)
43. Zhen B et al. *Phys. Rev. Lett.* **113** 257401 (2014)
44. Bulgakov E N et al. *J. Opt. Soc. Am. B* **35** 1218 (2018)
45. Jin J et al. *Nature* **574** 501 (2019)
46. Hsu C W et al. *Nature* **499** 188 (2013)
47. Fujita T et al. *Phys. Rev. B* **57** 12428 (1998)
48. Yablonskii A L et al. *J. Phys. Soc. Jpn.* **70** 1137 (2001)
49. Fan S, Joannopoulos J D *Phys. Rev. B* **65** 235112 (2002)
50. Tikhodeev S G et al. *Phys. Rev. B* **66** 045102 (2002)
51. Ochiai T, Sakoda K *Phys. Rev. B* **63** 125107 (2001)
52. Volya A, Zelevinsky V *Phys. Rev. C* **67** 054322 (2003)
53. Dicke R H *Phys. Rev.* **93** 99 (1954)
54. Mlynek J A et al. *Nat. Commun.* **5** 5186 (2014)
55. Cao H, Wiersig J *Rev. Mod. Phys.* **87** 61 (2015)
56. McEuen P "Nanostructures", in Kittel C *Introduction to Solid State Physics* 8th ed. (Hoboken, NJ: Wiley, 2005) p. 515, Ch. 18
57. Vincent P, Nevière M *Appl. Phys.* **20** 345 (1979)
58. Gao X et al. *Sci. Rep.* **6** 31908 (2016)
59. Bulgakov E N, Maksimov D N *Phys. Rev. A* **98** 053840 (2018)
60. Monticone F, Alù A *Phys. Rev. Lett.* **112** 213903 (2014)
61. Liberal I, Engheta N *Sci. Adv.* **2** e1600987 (2016)
62. Lepetit T, Kanté B *Phys. Rev. B* **90** 241103 (2014)
63. Pilipchuk A S, Pilipchuk A A, Sadreev A F *Phys. Scr.* **95** 085002 (2020)
64. Sadrieva Z F et al. *Phys. Rev. A* **99** 053804 (2019)
65. Yuan L, Lu Y Y *Phys. Rev. A* **102** 033513 (2020)
66. Gao X et al. *ACS Photon.* **6** 2996 (2019)
67. Wang Y et al. *J. Opt. Soc. Am. B* **33** 2472 (2016)
68. Kodigala A et al. *Nature* **541** 196 (2017)
69. Ndangali R F, Shabanov S V *J. Math. Phys.* **51** 102901 (2010)
70. Bulgakov E N, Sadreev A F *Phys. Rev. A* **90** 053801 (2014)
71. Jackson J D *Classical Electrodynamics* 2nd ed. (New York: Wiley, 1975)
72. Grahn P, Shevchenko A, Kaivola M *New J. Phys.* **14** 093033 (2012)
73. Miroshnichenko A E et al. *Nat. Commun.* **6** 8069 (2015)
74. Yang Y, Bozhevolnyi S I *Nanotechnology* **30** 204001 (2019)
75. Poshakinskiy A V, Poddubny A N *Phys. Rev. X* **9** 011008 (2019)
76. Shamkhi H K et al. *Phys. Rev. Lett.* **122** 193905 (2019)
77. Liu W, Kivshar Yu S *Opt. Express* **26** 13085 (2018)
78. Ruan Z, Fan S *Phys. Rev. Lett.* **105** 013901 (2010)
79. Ruan Z, Fan S *Appl. Phys. Lett.* **98** 043101 (2011)
80. Qian C et al. *Phys. Rev. Lett.* **122** 063901 (2019)
81. Krasikov S et al. *Phys. Rev. Appl.* **15** 024052 (2021)
82. Bohren C F, Huffman D R *Absorption and Scattering of Light by Small Particles* (New York: Wiley, 1983)
83. Sadrieva Z et al. *Phys. Rev. B* **100** 115303 (2019)
84. Mylnikov V et al. *ACS Nano* **14** 7338 (2020)
85. Ivchenko E L, Pikus G "Crystal symmetry", in *Superlattices and other Heterostructures*: *Symmetry and Optical Phenomena* (Springer Ser. in Solid-State Sciences, Vol. 110) (Berlin: Springer, 1995) p. 9, https://doi.org/10.1007/978-3-642-97589-9_2
86. Sakoda K *Optical Properties of Photonic Crystals* (Springer Ser. in Optical Sciences, Vol. 80) (Berlin: Springer, 2005)
87. Agranovich V M, Ginzburg V L *Crystal Optics with Spatial Dispersion, and Excitons* (Springer Ser. in Solid-State Sciences, Vol. 42) (Berlin: Springer, 2013); Translated from Russian: *Kristall-looptika s Uchetom Prostranstvennoi Dispersii i Teoriya Eksitonov* (Moscow: Nauka, 1979)
88. Dyakov S A et al. *Laser Photon. Rev.* **15** 2000242 (2021)
89. Overvig A C et al. *Phys. Rev. B* **102** 035434 (2020); arXiv:1903.11125
90. Doeleman H M et al. *Nat. Photon.* **12** 397 (2018)
91. Yoda T, Notomi M *Phys. Rev. Lett.* **125** 053902 (2020)
92. Bulgakov E N, Maksimov D N *Phys. Rev. Lett.* **118** 267401 (2017)
93. Bykov D A, Bezus E A, Doskolovich L L *Nanophotonics* **9** 83 (2019)
94. Liu W et al. *Phys. Rev. Lett.* **123** 116104 (2019)
95. Bulgakov E N, Sadreev A F *Phys. Rev. A* **96** 013841 (2017)
96. Huang C et al. *Science* **367** 1018 (2020)
97. Bai T et al. *Opt. Express* **29** 25270 (2021)
98. Wang B et al. *Nat. Photon.* **14** 623 (2020)
99. Webster M A et al. *IEEE Photon. Technol. Lett.* **19** 429 (2007)
100. Tummidi R S et al. "Anomalous losses in curved waveguides and directional couplers at 'magic widths'," in *LEOS 2008 — 21st Annual Meeting of the IEEE Lasers and Electro-Optics Society, Newport Beach, CA, USA, 09–13 November 2008* (Piscataway, NJ: IEEE, 2008) p. 521, https://doi.org/10.1109/LEOS.2008.4688721
101. Nguyen T G et al. *Laser Photon. Rev.* **13** 1900035 (2019)
102. Bezus E A, Bykov D A, Doskolovich L L *Photon. Res.* **6** 1084 (2018)
103. Azzam S I et al. *Phys. Rev. Lett.* **121** 253901 (2018)
104. Liang Y et al. *Nano Lett.* **20** 6351 (2020)
105. Sun S et al. *Phys. Rev. B* **103** 045416 (2021)
106. Koshelev K et al. *Phys. Rev. Lett.* **121** 193903 (2018)
107. Piper J R, Fan S *ACS Photon.* **1** 347 (2014)
108. Choi J M, Lee R K, Yariv A *Opt. Lett.* **26** 1236 (2001)
109. Pernice W H P et al. *Appl. Phys. Lett.* **100** 223501 (2012)
110. Seok T J et al. *Nano Lett.* **11** 2606 (2011)
111. Koshelev K et al. *ACS Photon.* **6** 1639 (2019)
112. Platte W, Sauerer B *IEEE Trans. Microwave Theory Tech.* **37** 139 (1989)
113. Makarov S et al. *Nano Lett.* **15** 6187 (2015)
114. Mazurenko D A et al. *Phys. Rev. Lett.* **91** 213903 (2003)
115. Liu Z et al. *Phys. Rev. Lett.* **123** 253901 (2019)
116. Hwang M-S et al. *Nat. Commun.* **12** 4135 (2021)
117. Chukhrov A et al. *Phys. Rev. B* **103** 214312 (2021)
118. Bulgakov E N, Pichugin K N, Sadreev A F *Opt. Express* **23** 22520 (2015)
119. Lannebère S, Silveirinha M G *Nat. Commun.* **6** 8766 (2015)
120. Sadrieva Z F et al. *ACS Photon.* **4** 723 (2017)
121. Bulgakov E N, Maksimov D N *Opt. Express* **25** 14134 (2017)
122. Bulgakov E N, Sadreev A F *Phys. Rev. A* **97** 033834 (2018)
123. Bulgakov E N, Sadreev A F *Phys. Rev. A* **94** 033856 (2016)
124. Pichugin K, Sadreev A, Bulgakov E *Nanophotonics* **10** 4341 (2021)
125. Sidorenko M S et al. *Phys. Rev. Appl.* **15** 034041 (2021)
126. Zakomirnyi V I et al. *Opt. Lett.* **44** 5743 (2019)
127. Romano S et al. *Materials* **11** 526 (2018)
128. Anthur A P et al. *Nano Lett.* **20** 8745 (2020)
129. Chen Z et al. *Sci. Bull.* **67** 359 (2022)

130. Ishizaki K, Okano M, Noda S *J. Opt. Soc. Am. B* **26** 1157 (2009)
131. Minkov M et al. *Opt. Express* **21** 28233 (2013)
132. Biberman A et al. *Opt. Lett.* **37** 4236 (2012)
133. Wolf P-E, Maret G *Phys. Rev. Lett.* **55** 2696 (1985)
134. Wiersma D S et al. *Nature* **390** 671 (1997)
135. Poddubny A N et al. *Nat. Commun.* **3** 914 (2012)
136. Limonov M F, De La Rue R M *Optical Properties of Photonic Structures*: *Interplay of Order and Disorder* (Boca Raton, FL: CRC Press, 2012)
137. Liu C et al. *Phys. Rev. Lett.* **123** 163901 (2019)
138. Galisteo-López J F et al. *Adv. Mater.* **23** 30 (2011)
139. Astratov V N et al. *Phys. Rev. B* **66** 165215 (2002)
140. Fan S, Villeneuve P R, Joannopoulos J D *J. Appl. Phys.* **78** 1415 (1995)
141. Lifshits I M, Gredeskul S A, Pastur L A *Introduction to the Theory of Disordered Systems* (New York: Wiley, 1988); Translated from Russian: *Vvedenie v Teoriyu Neuporyadochennykh System* (Moscow: Nauka, 1982)
142. Ni L et al. *Opt. Express* **25** 5580 (2017)
143. Maslova E E et al. *Nanophotonics* **10** 4313 (2021)
144. Chen H L, Wang G, Lee R K *Opt. Express* **26** 33205 (2018)
145. Rayleigh (Lord) *Philos. Mag.* **24** 145 (1887)
146. Elachi C *Proc. IEEE* **64** 1666 (1976)
147. Suhara T, Nishihara H *IEEE J. Quantum Electron.* **22** 845 (1986)
148. Magnusson R, Ko Y H "Guided-mode resonance nanophotonics: fundamentals and applications" *Proc. SPIE* **9927** 992702 (2016); in *Nanoengineering*: *Fabrication, Properties, Optics, and Devices XIII, Intern. Conf., San Diego, CA, August 30–31, 2016*
149. Chang-Hasnain C J, Yang W *Adv. Opt. Photon.* **4** 379 (2012)
150. Quaranta G et al. *Laser Photon. Rev.* **12** 1800017 (2018)
151. Qiao P, Yang W, Chang-Hasnain C J *Adv. Opt. Photon.* **10** 180 (2018)
152. Li L, in *Gratings*: *Theory and Numeric Applications* 2nd ed. (Ed. E Popov) (Marseille: Institut Fresnel, 2014) Ch. 13, p. 13.1
153. Botten L C et al. *Opt. Acta Int. J. Opt.* **28** 1087 (1981)
154. Weiss T, Muljarov E A *Phys. Rev. B* **98** 085433 (2018)
155. Neale S, Muljarov E A *Phys. Rev. B* **101** 155128 (2020)
156. Andreani L C, Gerace D *Phys. Rev. B* **73** 235114 (2006)
157. Modinos A, Stefanou N, Yannopapas V *Opt. Express* **8** 197 (2021)
158. Cotter N P K, Preist T W, Sambles J R *J. Opt. Soc. Am. A* **12** 1097 (1995)
159. Lalanne P, Hugonin J P, Chavel P *J. Lightwave Technol.* **24** 2442 (2006)
160. Karagodsky V, Chang-Hasnain C J *Opt. Express* **20** 10888 (2012)
161. Tishchenko A V *Opt. Quantum Electron.* **37** 309 (2005)
162. Karagodsky V, Chase C, Chang-Hasnain C J *Opt. Lett.* **36** 1704 (2011)
163. Ovcharenko A I et al. *Phys. Rev. B* **101** 155303 (2020)
164. Bykov D A, Bezus E A, Doskolovich L L *Phys. Rev. A* **99** 063805 (2019)
165. Parriaux O, Lyndin N M *J. Opt.* **21** 085608 (2019)
166. Weiss T et al. *J. Opt. Soc. Am. A* **28** 238 (2011)
167. Bykov D A, Doskolovich L L *J. Lightwave Technol.* **31** 793 (2013)
168. Whittaker D M, Culshaw I S *Phys. Rev. B* **60** 2610 (1999)
169. Krasnok A et al. *Adv. Opt. Photon.* **11** 892 (2019)
170. Blanchard C, Hugonin J-P, Sauvan C *Phys. Rev. B* **94** 155303 (2016)
171. Pietroy D et al. *Opt. Express* **15** 9831 (2007)
172. Neale S, Muljarov E A *Phys. Rev. B* **103** 155112 (2021)
173. Maystre D, Enoch S, Tayeb G, in *Electromagnetic Theory and Applications for Photonic Crystals* (Optical Science and Engineering, Vol. 102, Ed. K Yasumoto) (Boca Raton, FL: CRC Press, 2006) Ch. 1
174. Linton C M, McIver P *J. Eng. Math.* **30** 661 (1996)
175. Twersky V *J. Appl. Phys.* **23** 407 (1952)
176. Yuan L, Lu Y Y *J. Phys. B* **50** 05LT01 (2017)
177. Bulgakov E N, Maksimov D N *Phys. Rev. A* **96** 063833 (2017)
178. Yuan L, Lu Y Y *Phys. Rev. A* **95** 023834 (2017)
179. Snyder A W, Love J D *Optical Waveguide Theory* (New York: Springer, 2012) https://doi.org/10.1007/978-1-4613-2813-1
180. Bulgakov E, Sadreev A *Adv. Electromagn.* **6** (1) 1 (2017)
181. Kim S, Kim K-H, Cahoon J F *Phys. Rev. Lett.* **122** 187402 (2019)
182. Kim S, Cahoon J F *Acc. Chem. Res.* **52** 3511 (2019)
183. Meade R D et al. *J. Appl. Phys.* **75** 4753 (1994)
184. Johnson S G et al. *Phys. Rev. B* **60** 5751 (1999)
185. Fan S, Joannopoulos J D *Phys. Rev. B* **65** 235112 (2002)
186. Yang Y et al. *Phys. Rev. Lett.* **113** 037401 (2014)
187. Liang Y et al. *Phys. Rev. B* **84** 195119 (2011)
188. Rybin M V et al. *Phys. Rev. Lett.* **119** 243901 (2017)
189. Koshelev K, Kivshar Yu *Nature* **574** 491 (2019)
190. Han S et al. *Adv. Opt. Mater.* **9** 2002001 (2021)
191. Gandolfi M et al. *Phys. Rev. A* **104** 023524 (2021)
192. Odit M et al. *Adv. Mater.* **33** 2003804 (2021)
193. Melik-Gaykazyan E et al. *Nano Lett.* **21** 1765 (2021)
194. Silveirinha M G *Phys. Rev. A* **89** 023813 (2014)
195. Hayran Z, Monticone F *ACS Photon.* **8** 813 (2021)
196. Lepetit T et al. *Phys. Rev. B* **82** 195307 (2010)
197. Jacobsen R E et al. *ACS Photon.* **9** 1936 (2022)
198. Wiersig J *Phys. Rev. Lett.* **97** 253901 (2006)
199. Rybin M, Kivshar Yu *Nature* **541** 164 (2017)
200. Bogdanov A A et al. *Adv. Photon.* **1** 016001 (2019)
201. Chen W, Chen Y, Liu W *Laser Photon. Rev.* **13** 1900067 (2019)
202. Koshelev K, Kivshar Yu *ACS Photon.* **8** 102 (2021)
203. Pichugin K N, Sadreev A F *J. Appl. Phys.* **126** 093105 (2019)
204. Kolodny S, Iorsh I *Opt. Lett.* **45** 181 (2020)
205. Gladyshev S, Frizyuk K, Bogdanov A *Phys. Rev. B* **102** 075103 (2020)
206. Bulgakov E, Pichugin K, Sadreev A *Phys. Rev. A* **104** 053507 (2021)
207. Huang L et al. *Adv. Photon.* **3** 016004 (2021)
208. Yan W, Lalanne P, Qiu M *Phys. Rev. Lett.* **125** 013901 (2020)
209. Singh R et al. *Appl. Phys. Lett.* **99** 201107 (2011)
210. Zhang F et al. *Appl. Phys. Lett.* **105** 172901 (2014)
211. Fedotov V A et al. *Phys. Rev. Lett.* **99** 147401 (2007)
212. Campione S et al. *ACS Photon.* **3** 2362 (2016)
213. Vabishchevich P P et al. *ACS Photon.* **5** 1685 (2018)
214. Jain A et al. *Adv. Opt. Mater.* **3** 1431 (2015)
215. Ndao A e al. *Nanophotonics* **9** 1081 (2020)
216. Gorkunov M V, Antonov A A, Kivshar Yu S *Phys. Rev. Lett.* **125** 093903 (2020)
217. Gorkunov M V et al. *Adv. Opt. Mater.* **9** 2100797 (2021)
218. Overvig A, Yu N, Alù A *Phys. Rev. Lett.* **126** 073001 (2021)
219. Tittl A et al. *Science* **360** 1105 (2018)
220. Leitis A et al. *Sci. Adv.* **5** eaaw2871 (2019)
221. Foley J M, Young S M, Phillips J D *Phys. Rev. B* **89** 165111 (2014)
222. Foley J M, Phillips J D *Opt. Lett.* **40** 2637 (2015)
223. Cui X et al. *Sci. Rep.* **6** 36066 (2016)
224. Doskolovich L L, Bezus E A, Bykov D A *Photon. Res.* **7** 1314 (2019)
225. Gentry C M, Popović M A *Opt. Lett.* **39** 4136 (2014)
226. Midya B, Konotop V V *Opt. Lett.* **43** 607 (2018)
227. Ha S T et al. *Nat. Nanotechnol.* **13** 1042 (2018)
228. Wu M et al. *Nano Lett.* **84** (2020)
229. Azzam S I et al. *Laser Photon. Rev.* **15** 2000411 (2021)
230. Muhammad N et al. *Nano Lett.* **21** 967 (2021)
231. Yang J-H et al. *Laser Photon. Rev.* **15** 2100118 (2021)
232. Ignatyeva D O, Belotelov V I *Opt. Lett.* **45** 6422 (2020)
233. Chernyak A M et al. *JETP Lett.* **111** 46 (2020); *Pis'ma Zh. Eksp. Teor. Fiz.* **111** 40 (2020)
234. Zhen B et al. *Proc. Natl. Acad. Sci. USA* **110** 13711 (2013)
235. Sun T et al. *Sci. Rep.* **6** 27482 (2016)
236. Wang Y et al. *Biosensors Bioelectron.* **107** 224 (2018)
237. Meudt M et al. *Adv. Opt. Mater.* **8** 2000898 (2020)
238. Romano S et al. *J. Phys. Chem. C* **122** 19738 (2018)
239. Romano S et al. *Opt. Express* **27** 18776 (2019)
240. Wang Y et al. *Nanophotonics* **10** 1295 (2021)
241. Yesilkoy F et al. *Nat. Photon.* **13** 390 (2019)
242. Jahani Y et al. *Nat. Commun.* **12** 3246 (2021)
243. Bulgakov E N, Sadreev A F *Phys. Rev. B* **81** 115128 (2010)
244. Ndangali F R, Shabanov S V *Active Photon. Mater. V* **86** 88081F (2013)
245. Bulgakov E N, Sadreev A F *Opt. Lett.* **39** 5212 (2014)
246. Pichugin K N, Sadreev A F *J. Opt. Soc. Am. B* **32** 1630 (2015)
247. Pichugin K N, Sadreev A F *Phys. Lett. A* **380** 3570 (2016)
248. Wang T, Zhang X *Photon. Res.* **5** 629 (2017)
249. Krasikov S D, Bogdanov A A, Iorsh I V *Phys. Rev. B* **97** 224309 (2018)
250. Yuan L, Lu Y Y *SIAM J. Appl. Math.* **80** 864 (2020)
251. Deka J et al. *Opt. Lett.* **43** 5242 (2018)

252. Maksimov D N, Bogdanov A A, Bulgakov E N *Phys. Rev. A* **102** 033511 (2020)
253. Zograf G et al. *ACS Photon.* **9** 567 (2022)
254. Sinev I S et al. *Nano Lett.* **21** 8848 (2021)
255. Bahari B et al., arXiv:1707.00181
256. Yu Z et al. *Optica* **6** 1342 (2019)
257. Yu Z et al. *Nat. Commun.* **11** 2602 (2020)
258. Wang Y et al. *ACS Photon.* **7** 2643 (2020)
259. Henkel A et al., arXiv:2102.01686
260. Han S et al. *Adv. Mater.* **31** 1901921 (2019)
261. Mikheeva E et al. *Opt. Express* **27** 33847 (2019)
262. Bernhardt N et al. *Nano Lett.* **20** 5309 (2020)
263. Lochner F J F et al. *ACS Photon.* **8** 218 (2021)
264. Carletti L et al. *Phys. Rev. Lett.* **121** 033903 (2018)
265. Carletti L et al. *Phys. Rev. Res.* **1** 023016 (2019)
266. Kolodny S A, Kozin V K, Iorsh I V *JETP Lett.* **114** 124 (2021); *Pis'ma Zh. Eksp. Teor. Fiz.* **114** 154 (2021)
267. Poddubny A N, Smirnova D A, arXiv:1808.04811
268. Romano S et al. *Photon. Res.* **6** 726 (2018)
269. Koshelev K, Bogdanov A, Kivshar Yu *Sci. Bull.* **64** 836 (2019)
270. Timofeev I V, Maksimov D N, Sadreev A F *Phys. Rev. B* **97** 024306 (2018)
271. Pankin P S et al. *Sci. Rep.* **10** 13691 (2020)
272. Pankin P et al. *Commun. Phys.* **3** 91 (2020)
273. Wu B-R et al. *Laser Photon. Rev.* **15** 2000290 (2021)
274. Tong H et al. *Nat. Commun.* **11** 5216 (2020)
275. Deriy I et al. *Phys. Rev. Lett.* **128** 084301 (2022)
276. Huang S et al. *Phys. Rev. Appl.* **14** 021001 (2020)